BODY FORCE OF A PLASMA ACTUATOR WITH DIFFERENT OPERATING CONDITIONS USING A PHASE-RESOLVED APPROACH

VENUR TEJAS ALVA

A THESIS SUBMITTED TO THE FACULTY OF GRADUATE STUDIES
IN PARTIAL FULFILMENT OF THE REQUIREMENTS
FOR THE DEGREE OF
MASTER OF APPLIED SCIENCE

GRADUATE PROGRAM IN MECHANICAL ENGINEERING
YORK UNIVERSITY
TORONTO, ONTARIO

MARCH 2021

Abstract

Plasma actuators are a type of electric device that can generate a flow of air without any moving parts. The salient feature of a plasma actuator is its ability to impart a body force in the region of the ionized air. The force produced is unsteady and it varies at the time scale of the input oscillating voltages (on the order of kHz) required to operate the actuator. While the force is often treated as steady in computations, the unsteady forcing is important for applications that require high frequency input. A phase-resolved determination of force distribution and total magnitude is important to develop models that better approximate physical conditions for use in numerical simulations and design.

Phase resolved study of the body force generated by the plasma actuator is performed experimentally using Particle Image Velocimetry. The primary objective of the present work is to study the ability of plasma actuators to transfer momentum to the air and the contribution of terms in the momentum equations used to compute the body force from the planar flow field measurements. The spatial and temporal evolution of the effect of the forcing by the actuator has been discussed with emphasis on the local acceleration term from the momentum equation. In addition, the effect of the voltage and the frequency of the driving signal of the plasma actuator on the spatial distribution of the volume force terms is studied.

In this thesis, the effect of phase resolution on the volume force terms caused by the operation of the plasma actuator is explored. The data were acquired for operating voltages, V_{pp} = 7-9 kV and frequency, f = 1-3 kHz, at 8 phases, 16 phases, and 32 phases within the actuation cycle. It is found that the phase resolution during data acquisition has a significant effect on the spatial distribution and the magnitude of the force.

Acknowledgement

First of all I would like to express my deepest gratitude to Dr. Ronald Hanson for giving me an opportunity to complete my graduate studies at York University in the Fluid Mechanics and Flow Control (FMFC) lab. This work wouldn't be possible without his constant support and guidance. I would also like to thank him for being a role model, and an inspiration to pursue excellence throughout my career.

I owe a debt of gratitude to Dr. Philippe Lavoie for granting me access to perform my experiments at University of Toronto Institute for Aerospace Studies (UTIAS) in the Flow Control and Experimental Turbulence (FCET) lab. His role as a supportive mentor was of immense value to me.

I would like to thank my friends at FMFC lab and FCET lab for providing a friendly and encouraging environment to work in.

I am grateful to my masters supervisory committee members, Drs. Garrett Melenka, Roger Kempers and Shooka Karimpour, for their insights that helped improve this thesis.

On a personal note, I would like to express my deepest thanks to my dad, Ajith, my mom, Shobha and my brother, Shreyas, for believing in me and supporting my decisions throughout my life. Finally, I am grateful to all my mentors and friends for their encouragement and support.

Table of Contents

List of Figures

List of Tables

Chapter 1

Introduction

1.1 Motivation

With an increasing emphasis on efficiency of aerial vehicles in the aviation industry, passive methods of controlling the flow have been pushed to the limits, and no longer yield further improvements. This has led to an increased interest in the development of active flow methods [1]. The ability to adapt easily to changing operating conditions, is the key in further improving the efficiency of air flow control. A type of actuator that has piqued interest in the last few years are surface Dielectric Barrier Discharge plasma actuators [1, 2]. Several studies have shown the applicability of these actuators in flow control situations such as delaying flow transition and drag reduction [3, 4]. Plasma actuators posses the ability to add momentum to the surrounding air, while having a very short response time and operating at an order of tens of kilo-hertz. A combination of these factors have primarily motivated the researchers to improve their understanding of these devices and develop them further. The motivation of the present work is to add to this understanding of operation and characterization of plasma actuators.

Active flow control methods are only as effective as the actuator being used. For most actuators, their effectiveness is judged by their ability to transfer momentum to the surrounding

air. The primary objective of the present work is to study the ability of the plasma actuator to impart this momentum, which leads to a wall jet. An effort is made to add to the understanding of the origin of the force by looking into its spatial and temporal evolution. This is done by performing flow field measurements above the plasma actuator, in a phase-resolved approach using Particle Image Velocimetry. Phase-resolved measurements help study the unsteady characteristics of the flow within the actuation cycle [5]. Using phase-resolved measurements, data acquisition system operating at a much lower frequency than the actuator can be used, as the data can be acquired at particular phase of actuation and phase averaged over several cycles. The effect of operating voltage and frequency of the plasma actuator on its ability to transfer momentum is also investigated. To better understand the effectiveness of the plasma actuator, it is important to study its functioning within an actuation cycle and over several cycles of actuation. Performing flow measurements at more instances in the actuation cycle helps understand the development of the force. This leads us to the second objective of the present work, where the effect of resolving the actuation cycle at different number of phases is studied. Overall, the present work aims to characterize the force generated by plasma actuator, as well as an effective way to capture it.

1.2 Organization of Thesis

Chapter 2 provides a brief introduction to the working principle and physics behind the plasma actuator. A description of wall jets is also provided. This is followed by a review of operational trends and applications of plasma actuators. The details of the plasma actuator used in the present work, and experimental setup for flow measurements is discussed in Chapter 3, along with the methodology of data acquisition and data processing. Results of the flow field measurements over the plasma actuator are shown and discussed in Chapter 4. In Chapter 5, the effect of phase resolution on the computed body force are presented. Finally, concluding remarks are made in Chapter 6.

Chapter 2

Background

2.1 Plasma Actuators

Plasma actuator is a general term used to describe several types of plasma based control devices [6]. *Plasma* is defined as a state of matter which is gaseous in nature consisting of ions and free electrons. The term *plasma actuator* is used to denote a Dielectric-Barrier-Discharge (DBD) plasma actuator, a subset of plasma actuators, that is considered in the present work. Roth *et al.* [7] are credited with initially developing a DBD plasma actuator and demonstrating their potential as flow control devices. Since then, plasma actuators have received alot of interest in the scientific community and efforts have been made to optimize performance [8].

2.2 DBD Plasma Actuator Physics

DBD plasma actuators consists of a two asymmetric electrodes separated by a dielectric layer [9]. The grounded electrode is encapsulated by the dielectric layer and the exposed electrode is placed over it as shown in Figure 2.1. A high-voltage, high-frequency AC current is used to operate the plasma actuator as DC current fails to pass through the dielectric barrier [10].

Plasma actuators are typically operated in the voltage range of 1 - 50 kV and frequencies ranging between 0.5 - 10 kHz.

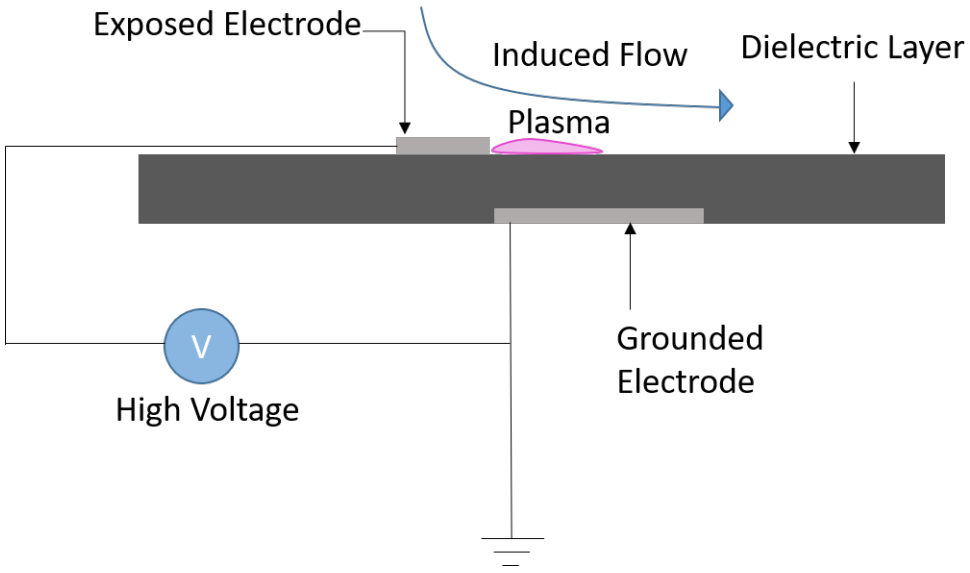

Figure 2.1: Schematic of a DBD plasma actuator showing the main components, depicted region of plasma and the induced airflow.

High voltage AC signal applied across the electrodes, creates an electric field between them and thereby weakly ionizing the air over the dielectric layer leading to the formation of plasma near the exposed electrode. The plasma created, consisting of highly energized ions and free electrons, transfers its momentum to the ambient air through particle-particle collision within a strong electric field. This transfer of momentum is referred to as *body force*. The body force leads to the formation of a wall bounded flow, in the downstream direction of the actuator in the form of a wall jet.

The dielectric medium is a material with low electric conductivity. Hence, the current does not pass through the medium but does polarize it. It has been well known that the plasma actuator has an asymmetric current response to the symmetric AC signal supplied [11].

During the negative half cycle, the exposed electrode becomes the cathode with abundant negative charge. The strong electric field between the electrode forces electrons out of the exposed electrode. The electrons move towards the grounded electrode and accumulates on

the surface, as depicted in Figure 2.2(a). This accumulation of charges decreases the strength of the electric field and favours the creation of negative charges [12].

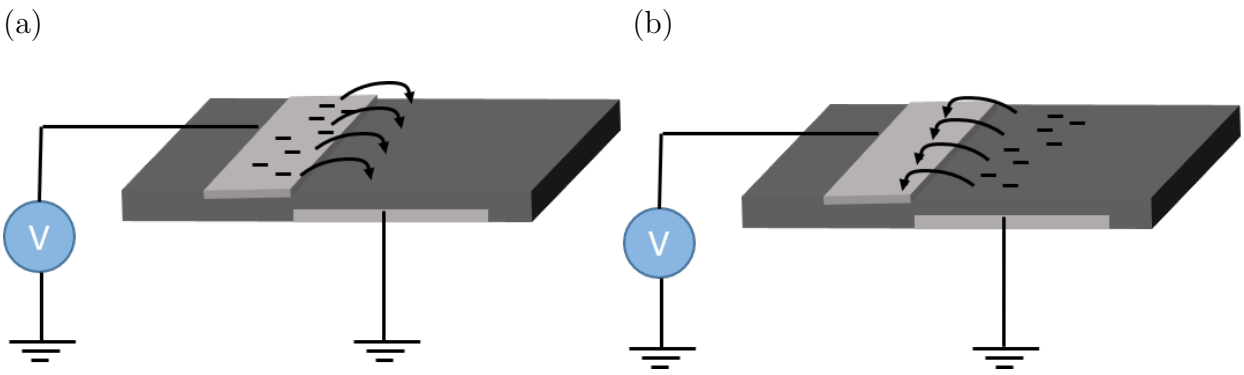

Figure 2.2: Description of ion drift during (a) Negative half cycle and, (b) Positive half cycle of actuation.

During the positive half cycle, the exposed electrode switches to being an anode. The free electrons on the surface of the dielectric are absorbed by the exposed anode, as shown in Figure 2.2(b). This increases the strength of the electric field and increases the momentum of the electrons moving towards the anode. The moving electrons tend to ionize the air through electron collision in the process. This leads to the formation of the positively charged ions in the vicinity of the anode. These positively charged ions are rejected by the exposed anode and move towards the grounded electrode [12].

Since an AC voltage is applied to the actuator, the electric field constantly changes direction. There has been two theories trying to explain the momentum transfer in plasma actuators, the push-pull theory and the push-push theory. The push-pull theory suggests that the body force is a result of a strong push or acceleration of the flow in the downstream direction in one half cycle of actuation, and a weak pull or deceleration of the flow in the other half cycle, leading to a net push in the downstream direction [13, 14] .The push-push theory on the other hand suggests a possibility that the plasma actuator pushes or accelerates the air in both halves of the actuation cycle, also leading to net acceleration in the downstream direction [15, 16].

However it is important to state that the generally held view is that the magnitude of force generated by the plasma actuator is higher in the negative half cycle of actuation and is supported by the work shown in Kriegseis *et al.* [1] and Benard *et al.* [17].

2.3 Advantages and Disadvantages of Plasma Actuators

The DBD plasma actuators have been of great interest for researchers due to their potential applications in air flow control. The plasma actuators however have their own advantages and disadvantages as compared to other actuators, which are discussed by Cattafesta and Sheplak [2].
The advantages of plasma actuators include:

- **No moving parts:** One of the biggest advantages of plasma actuators are the lack of moving parts. This greatly reduces the design complexities as compared to other systems with moving parts.
- **Fast time response:** The ability to control air flow over a surface considerably depends on the rate at which the actuator can respond. As plasma actuators operate over a wide frequency range their responses can be controlled to be quick.
- **Low system mass and easier construction:** The assembly of the plasma actuators is a simple process and usually done with hand. This reduces the time required to manufacture as compared to complex air flow control devices. As the plasma actuator itself primarily consist of two electrodes, and a dielectric barrier, they tend to be very low in weight.

As with most devices, plasma actuators have their own disadvantages. They are as follows:

- **High voltage:** A high voltage, in the order of kilovolts, is required to operate the plasma actuators. A high voltage is required because of the dielectric barrier present

between the electrodes and to maintain a strong electric field across it. Optimization of the dielectric barrier thickness can improve the efficiency of the actuator and reduce the operating voltage required.

- **Limited induced velocity:** The velocity induced by the actuator is limited and can not be increased beyond a certain limit Forte *et al.* [18] and Roth *et al.* [19] made an effort to find the maximum force the plasma actuator can generate for a given operating voltage. The maximum velocity that could be achieved was estimated to be approximately 8 m/s [1].

2.4 Applications of Plasma Actuators

Moreau [6] outlined that the plasma actuators can generally be used in flow control to modify three flow phenomena: laminar-to-turbulent transition, flow separation and wake control. Grundmann and Tropea [20] demonstrated the potential application of using plasma actuators in airflow control by using them to suppress the Tollmien-Schlichting waves and thereby delaying the transition to turbulent flow. Hanson *et al.* [3] demonstrated the ability to control the disturbances in the flow experiencing transient growth, and thereby delaying the transition to turbulence. Seraudie *et al.* [4] further showed the ability of the plasma actuator to delay the laminar-to-turbulent transition in the flow. The capacity of plasma actuators to mitigate flow-induced noise was demonstrated by Huang *et al.* [21]. Jolibois *et al.* [22] and Patel *et al.* [23] were successful in showing that the plasma actuators can be used to control flow separation over airfoils. Kozlov and Thomas [24] demonstrated that plasma actuators can also be used in wake control, by using them to control vortex shedding on bluff bodies. Apart from external flow, Lemire *et al.* [25] and Li *et al.* [26] have used plasma actuators to control internal flows as well. More recent studies have also looked into the application of plasma actuator in supersonic flow control [27]. Further details of the applications of plasma actuators can be found in overviews presented by Kriegseis *et al.* [1] and Cattafesta *et al.* [2].

2.5 Wall Jet

The formation of a wall jet is an important characteristic of plasma actuators. The plasma actuator in quiescent conditions transfers momentum into the air directly above the electrodes. This transfer of momentum through particle-particle collision accelerates the flow downstream, tangentially to the wall. This leads to a suction effect over the electrodes and directs the air towards them, leading to a quasi steady wall jet.

Wall jet can simply be defined as a jet of fluid flowing tangentially along a wall. It is considered to be a special form of free jet wherein the wall jet can be imagined as the flow occurring if a thin plate is inserted in along the plane of symmetry of free jet .

Wall jets can be classified by their geometries, radial or planar and by the Reynolds number, laminar or turbulent [28]. A planar wall jet is bound by a wall in the direction of the flow (eg., flow through a sluice). A radial wall jet is bound by wall extending radially in the direction of the flow (eg., water from a tap impinging onto the sink).

A wall jet profile is divided into two regions with the location of the maximum velocity from the wall as a reference. The region above and below the location of the maximum velocity is known as the *Outer region* and *Inner region* respectively as depicted in Figure 2.3.

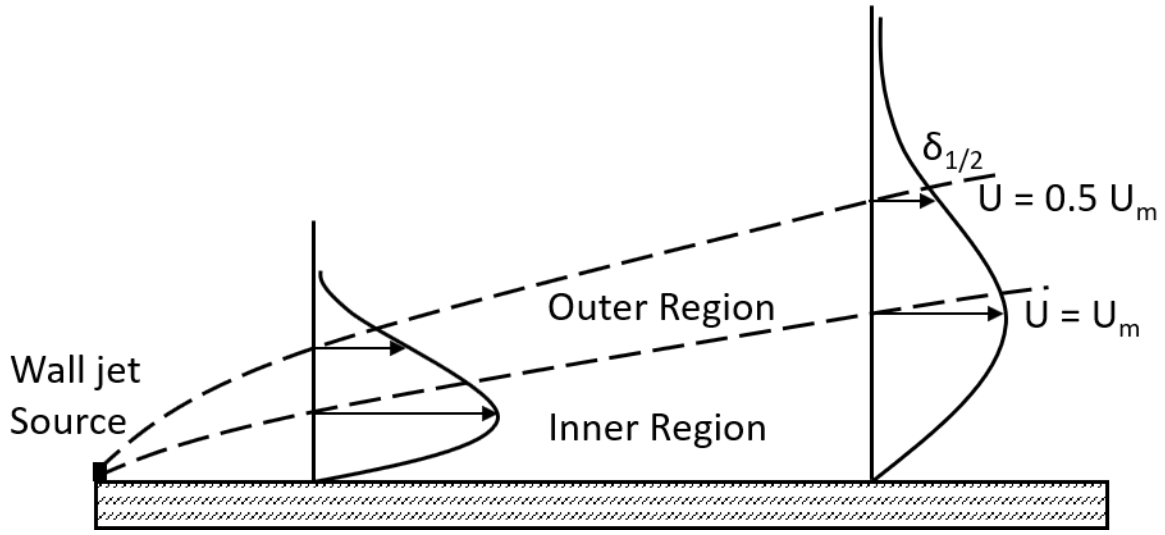

Figure 2.3: Schematic description of wall jet profile, where U denotes the velocity.

The half jet width, $\delta_{1/2}$, is a parameter often used to characterize a wall jet along with the maximum velocity magnitude in the profile. It is defined as the point where the velocity reduces to half the maximum velocity over the point of maximum velocity.

2.6 Wall Jet Equations

From a flow control point of view, an important characteristic of a plasma actuator is its ability to generate a wall jet.

Glauert [28] derives the solution for a laminar jet flowing over a plane wall, which can be used to predict the velocity distribution of the wall jet generated by the plasma actuator. In solving for the similarity solutions for a wall jet, Glauert suggests treating the region close to the wall using boundary layer approximations on momentum and continuity equations and deducing a integral relation from the same equations for the region away from the wall.

Considering the boundary layer approximation, the pressure is assumed to be constant and the momentum equation is given to be

$$u\frac{\partial u}{\partial x} + v\frac{\partial u}{\partial y} = \nu\frac{\partial^2 u}{\partial^2 y}, \tag{2.1}$$

where x and y are the distances along the wall and normal to the wall respectively. The terms u and v denote the corresponding velocity components in the x and y directions, while ν denotes the kinematic viscosity.

The continuity equation for incompressible flow is

$$\frac{\partial u}{\partial x} + \frac{\partial v}{\partial y} = 0 \tag{2.2}$$

Which is satisfied by stream function ψ , such that,

$$u = \frac{\partial \psi}{\partial y}, \qquad v = -\frac{\partial \psi}{\partial x}. \tag{2.3}$$

The boundary conditions are

$$u = v = 0 \ at \ y = 0, u \to 0 \ as \ y \to \infty. \tag{2.4}$$

Upon using non dimensional form of terms, u, v, x, y, ψ, Equation 2.1 can be reduced to,

$$f''' + ff'' + \alpha f'^2 = 0. \tag{2.5}$$

The boundary conditions (2.4) require that,

$$f(0) = f'(0) = 0, \ \ f'(\infty) = 0,$$

where f, represents the mass flux, f' the velocity and η the normalized distance from the wall.

Upon further investigation, Glauert found that $\alpha = 2$ satisfies the boundary conditions and there by showing the equation for f to be,

$$f''' + ff'' + 2f'^2 = 0, \tag{2.6}$$

with boundary conditions $f(0) = f'(0) = 0, \ \ f'(\infty) = 0.$

By multiplying Equation 2.6 by f and integrating the first term by parts, arrives at

$$ff'' - \frac{1}{2}f'^2 + f^2 f' = 0, \tag{2.7}$$

Further multiplying by $f^{-3/2}$ and integrating again gives,

$$f^{-\frac{1}{2}}f' + \frac{2}{3}f'^{\frac{3}{2}} = constant. \tag{2.8}$$

Glauert to further simplify the solving of the equation, substitutes $f = g^2$, then f' becomes $f' = 2gg'$ and Equation 2.8 becomes,

$$g' = \frac{1}{3}(1 - g^3), \tag{2.9}$$

which on integration gives,

$$\eta = \log \frac{\sqrt{1 + g + g^2}}{1 - g} + \sqrt{3} tan^{-1} \frac{\sqrt{3g}}{2 + g}. \tag{2.10}$$

Then the values of η, f and f' for given values of g is tabulated. The variation of f and f' with η are shown in Figure 2.4.

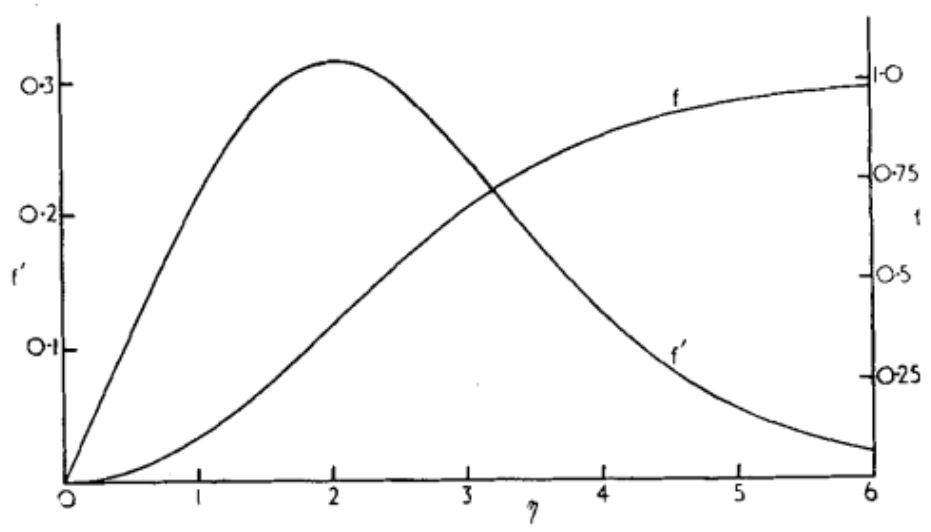

Figure 2.4: Laminar wall jet profile. Variation of mass flux (f) and velocity (f') with distance from the wall. Reprinted with permission from Glauert [28].

2.7 Body Force

In this section, various methods that have been used to determine the body force in the past studies is discussed. The velocity fields were acquired using techniques like Particle Image Velocimetry (PIV), to which several integral and differential methods have been applied to calculate the force distribution and the resulting body force, as found in Versailles *et al.* [29], Wilke [30] and Albercht *et al.* [31] as examples.

Integral methods have been used to conveniently calculate the actuator force based on the so-called Control Volume Analysis. Using this technique, the momentum balance equation is applied across a Control Volume (CV), viz.

$$\frac{D}{Dt}\iiint_{V(t)} \rho u \, dV = \iiint_{V(t)} \rho k \, dV + \iint_{S(t)} \rho t \, dS, \tag{2.11}$$

where u is the velocity, k is the mass body force and t is the stress vector.

A control volume, in the present context, can be defined as an area across which the net force added by the plasma actuator is calculated. Figure 2.5, depicts a typical CV arbitrarily applied over a plasma actuator during flow calculations. The left (line a-b), right (line c-d) and the top (line b-c) boundaries of CV are also shown, along with the wall (line a-d).

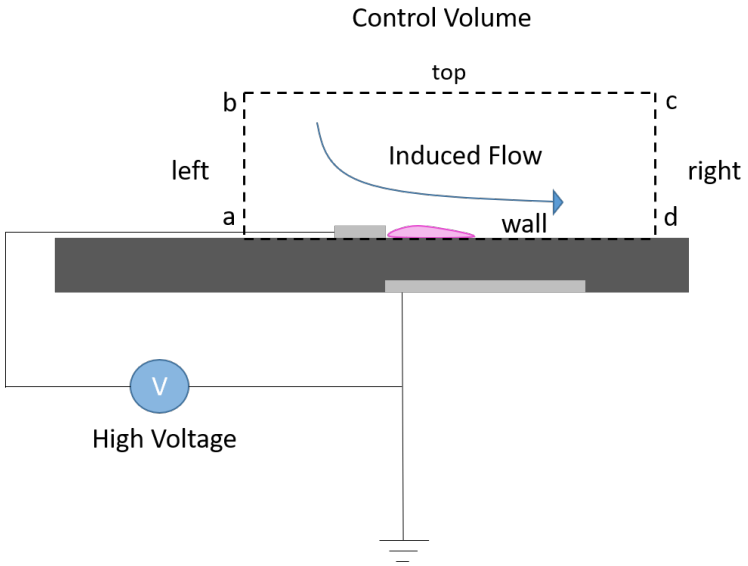

Figure 2.5: Schematic of an arbitrary control volume over a plasma actuator.

For an incompressible, 2D steady flow, the above momentum-balance equation, reduces to

$$\frac{F}{L} = \rho \int_{right} u^2 \, dy - \rho \int_{left} u^2 \, dy + \rho \int_{top} uv \, dx + \int_{wall} \tau_w \, dx, \tag{2.12}$$

where, F/ L is the actuator force per unit length in the x-direction. The above equation has been simplified previously based on the available measurement technique, and the degree of simplification results into four different cases (1-4) of integral methods, briefly described below as in Kriegseis *et al.* [32].

Case 1: Versailles *et al.* [29] processed their PIV data by using the exact, reduced momentum-balance equation. Where the shear stress was calculated using the first data point above the wall, according to

$$\tau = \mu \frac{\triangle u}{\triangle y}. \tag{2.13}$$

Substituting Equation 2.13 into Equation 2.12 leads to,

$$\frac{F}{L} = \rho \int_{right} u^2 \, dy - \rho \int_{left} u^2 \, dy + \rho \int_{top} uv \, dx + \int_{wall} \frac{\triangle u}{\triangle y} \, dx. \tag{2.14}$$

Case 2: Another approach is to calculate the momentum flux across the CV boundaries as shown by Durscher and Roy [33] according to

$$\frac{F}{L} = \rho \int_{right} u^2 \, dy - \rho \int_{left} u^2 \, dy + \rho \int_{top} uv \, dx. \tag{2.15}$$

The force calculated is the net force, viz.

$$F = F_{plasma} - F_{friction}. \tag{2.16}$$

Case 3: Based on pitot-tube measurements, Hoskinson *et al.* [34, 35], assumed the flux over the top and left CV boundaries to be negligible and further neglected the wall shear. Thereby reducing the equation to,

$$\frac{F}{L} = \rho \int_{right} u^2 \, dy. \tag{2.17}$$

Case 4: Baughn *et al.* [36] concluded that the flux through the left boundary was unaffected by the presence of the actuator and thereby chose to neglect it and compute the force by,

$$\frac{F}{L} = \rho \int_{right} u^2 \, dy + \rho \int_{top} uv \, dx + \int_{wall} \frac{\triangle u}{\triangle y} \, dx. \tag{2.18}$$

To better understand the spatial distribution of the body force, differential methods used by Wilke *et al.* [30] and Albercht *et al.* [31] are described next as case 5 and 6, respectively.

Case 5: Wilke *et al.* [30] proposed applying the Naiver stokes equations for steady and incompressible 2D flows. In order to calculate the force terms, Wilke assumes (and retroactively verifies) that the order of magnitude is at least an order greater than the pressure gradient, i.e,

$$f \gg \frac{\partial p}{\partial x}. \tag{2.19}$$

Consequently, the pressure gradients are ignored, i.e,

$$\frac{\partial p}{\partial x} = 0. \tag{2.20}$$

And thereby the body force terms are given by f_x and f_y as follows:

$$f_x(x,y) = \rho(u\frac{\partial u}{\partial x} + v\frac{\partial u}{\partial y}) - \mu(\frac{\partial^2 u}{\partial x^2} + \frac{\partial^2 u}{\partial y^2}), \tag{2.21}$$

$$f_y(x,y) = \rho(u\frac{\partial v}{\partial x} + v\frac{\partial v}{\partial y}) - \mu(\frac{\partial^2 u}{\partial x^2} + \frac{\partial^2 u}{\partial y^2}). \tag{2.22}$$

Case 6: Albrecht *et al.* [31] used the vorticity equation to circumvent the problem of unknown pressure gradients and estimate the body forces according to

$$\frac{1}{\rho}(\frac{\partial f_x}{\partial y} - \frac{\partial f_y}{\partial x}) = u\frac{\partial \omega}{\partial x} + v\frac{\partial \omega}{\partial y} - \frac{\mu}{\rho}(\frac{\partial^2 \omega}{\partial y^2}), \tag{2.23}$$

where,

$$\omega = \frac{\partial v}{\partial x} - \frac{\partial u}{\partial y}. \tag{2.24}$$

Albrecht assumed that vorticity was strongly dominated by $\frac{\partial f_x}{\partial y}$ and $\frac{\partial f_y}{\partial y}$ was thus neglected. The resulting equation after integration was,

$$f_x(x,y) = -\rho \int_0^\infty [u\frac{\partial w}{\partial x} + v\frac{\partial w}{\partial x} + v\frac{\partial w}{\partial y} - \frac{\mu}{\rho}(\frac{\partial^2 w}{\partial x^2} + \frac{\partial^2 w}{\partial y^2})]\, dy. \tag{2.25}$$

Kriegseis *et al.* [32] compared the body force per unit length of the plasma actuators obtained using the various approaches stated above. The comparison of the approaches appear in color and the balance based data in grey in Figure 2.6. The differential methods, shown by case 5 (in yellow) and 6 (in blue), seem to be in good agreement with each other, and thereby support the assumptions made by Wilke [30] and Albrecht [31].

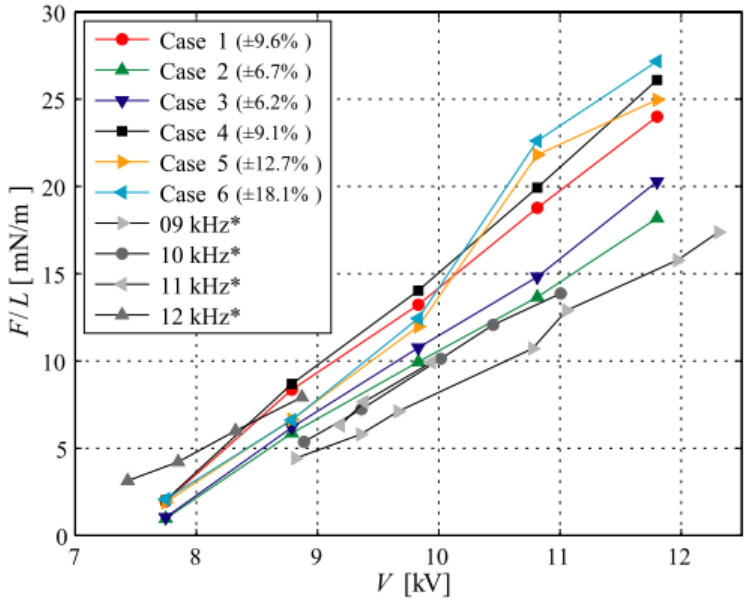

Figure 2.6: Variation of plasma actuator force along with operating voltage; implemented Cases 1-6 are represented in color, balance based data is represented in grey. Reprinted with permission from Kriegseis *et al.* [32].

2.8 Time Resolved Body Force and Acceleration Terms

For most applications of plasma actuators the body force is assumed steady, as is the case in the aforementioned analysis (cases 1 to 6). However, it has been observed that the body force over a single actuation cycle is not constant, and efforts have been made to characterize the unsteady body force [37, 17]. Kotsonis *et al.* [38], applied the Navier-Stokes(NS) equations to the velocity field to determine the body force. The 2D incompressible NS equation including the body force term is

$$\underset{(1)}{\frac{\partial U}{\partial t}} + \underset{(2)}{U \cdot \nabla U} - \underset{(3)}{\nu \nabla^2 U} = \underset{(4)}{-\nabla p} + \underset{(5)}{\frac{F}{\rho}}, \tag{2.26}$$

where U is the 2D velocity field, ∇p is the pressure gradient, ν is the kinematic viscosity, F is the body force and ρ is the density. The first, second and third term on the left-hand side

of Equation 2.26 are the local acceleration term, the convective term and the viscous term, respectively. On the right-hand side of the Equation 2.26, the fourth and fifth term of the equation, denoting the pressure term and the body force term respectively, is shown.

In the pursuit of deriving the body force through Navier-Stokes equations, it becomes necessary to calculate all the other terms involved i.e, the local acceleration, convective and viscous terms. These terms can be calculated using the spatio-temporal data acquired.

Benard *et al.* [17], used the discretized form of momentum equations for 2D incompressible flow to determine the contribution of each term of the momentum equations in the magnitude of the body force, shown in Figure 2.7. It was observed that during an actuation cycle, the local acceleration term (eq. 2.26 term (1)) was a dominant factor in production of the unsteady body force as depicted in Figure 2.7. It can be seen that the trend of the total body force follows a trend similar to that of the local acceleration term. The convective term (eq. 2.26 term (2)) was measured to be an order of magnitude lower than the local acceleration term. Benard *et al.* [17] observed that the magnitude of the convective term was nearly constant throughout the actuation cycle. The contribution of the viscous term (eq. 2.26 term (3)) was observed minimal and restricted only within the boundary layer.

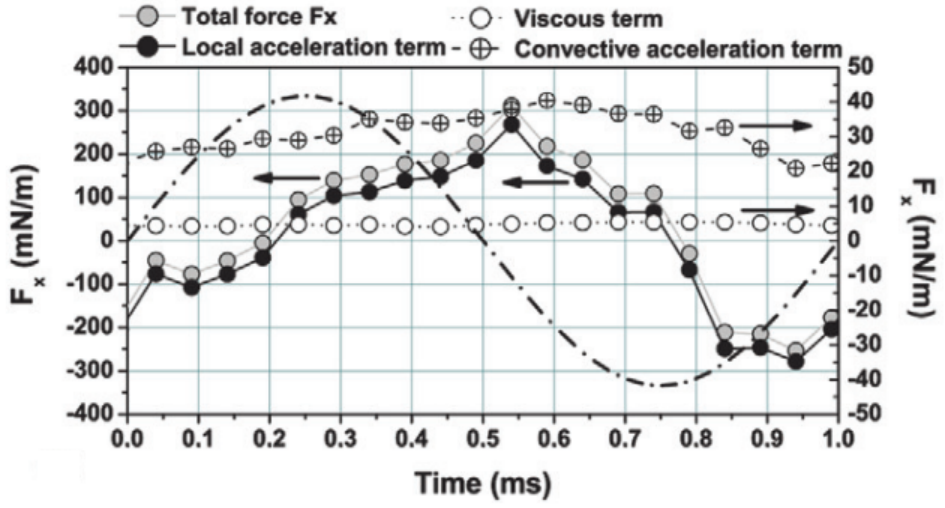

Figure 2.7: Separate contributions of each of the terms of the Navier Stokes Equations. The dashed–dotted line is the applied voltage to the actuator. Reprinted with permission from Benard *et al.* [17]

Benard *et al.* [17] also studied the contribution of the terms of momentum equation (eq. 2.26) to the time averaged body force over a number of actuation cycles. It was found that the convective term mean body force was largely governed by the convective term and the local acceleration and viscous terms had a negligible contribution.

The pressure term (eq. 2.26 term (4)) requires the measurement of the pressure field that cannot be measured directly. Several methods have been proposed to calculate the pressure term like derivation of the momentum equations or solving the pressure Poisson equation. Albrecht *et al.*. [31], worked around the problem by using the Vorticity equation to compute the body force. Debien *et al.* [39, 40], computed the time resolved spatially integrated body force using time resolved velocity fields without making any assumptions over the pressure term and including it in force calculation. Wilke [30] and Neumann *et al.* [41] made the assumption that the pressure term was less significant in the vicinity of the discharge as compared to the other terms and thereby neglecting the pressure term. Benard *et al.* [17], draws comparison between temporal evolution of the body force presented by Debien *et al.* [39, 40], Wilke [30] and Neumann *et al.* [41]. It was observed that the two different methods, lead to similar time evolutions of the total body force. Therefore, though Benard *et al.* [17] confirms the presence of a pressure gradient, the work concluded that the contribution of the term is indeed insignificant. For this reason, the pressure gradient term in this present study has been neglected.

2.9 Geometric Parameters Affecting Force Generation

The dielectric layer in between the electrodes is a physical characteristic of a DBD plasma actuator. The effect of the thickness of the dielectric layer on the induced velocity was studied by Forte *et al.* [18]. It was observed that the induced velocity increased with the decrease in the dielectric layer thickness. This is attributed to a stronger electric field as a result of reducing the barrier between the electrodes. Therefore, reducing the thickness of the dielectric layer was seen to have the same effect as increasing the permittivity or the

operating voltage [18]. Thomas *et al.* [42] showed that it might be better to use thicker dielectrics with lower dielectric coefficients as they result in lower power losses.

Forte *et al.* [18] also studied the effect of different dielectric materials in plasma actuators, by comparing the power consumption of actuators with glass and acrylic (PMMA) dielectrics. It was found that the actuator with glass dielectric produced higher velocity than the actuator with PMMA dielectric at lower voltages and then produced velocities smaller than PMMA actuator at higher voltages. Glass, with higher permittivity than PMMA, was expected to produced higher velocities as the electric field would be stronger. While this held true for lower voltages, the discharge produced by the glass actuator was observed to become more filamentary and unstable at higher voltages, resulting in lower velocities.

Enloe *et al.* [8] studied the effect of the width of the insulated electrode on the magnitude of velocity induced. It was observed that with increasing width of the insulated electrode, the induced velocity also was higher. However, there would be an optimum width of the electrode beyond which no significant improvement in the performance of the actuator is observed.

Enloe *et al.* [8] further observed that the width of the exposed electrode had negligible effect on the actuator performance, whereas its thickness had a significant effect on the actuator's efficiency. The thinner electrode was more efficient in converting input power into body force.

The effect of horizontal distance between the electrodes was also studied by Forte *et al.* [18]. It was found that the velocity induced increased upon increasing the distance between the electrodes. However, it was observed that the velocity decreased beyond an optimum inter electrode gap, as increasing the distance beyond it, weakened the electric field between the electrodes.

The frequency and voltage applied to the plasma actuators are crucial operating parameters. Their effect on the magnitude of velocity induced provides an understanding of the threshold of the plasma actuator effectiveness. Forte *et al.* [18] found that the maximum velocity

induced by the plasma actuator increased with an increase in the actuation frequency. It was suggested that the reason for this could be that the mean number of particle collisions increase with increase in actuation frequency, leading to an increase in the velocity induced. However, this effect of frequency on the maximum velocity held true until a threshold value of frequency was reached, beyond which the maximum velocity reached a plateau. Typically the surface of the dielectric is charged and relaxed at the ignition of discharge during an actuation cycle. The reason for the plateauing of maximum velocity beyond the threshold frequency was assumed to be the lack of relaxation time for the charged surface.

Forte *et al.* [18] also observed that the maximum velocity induced increased with the increase in the operating voltage and did not plateau after a given voltage value. This suggested that the maximum induced velocity can continue to increase with higher voltage supplies until the dielectric breaks down.

2.10 Power Consumption

The velocity of the induced wall jet is dependent on the voltage applied to the actuator system. So, energy consumed by the actuator system can be related to the capacity of the plasma actuator to transfer the momentum to the surrounding air.

There are two ways to determine the power consumed by the actuator, that is either through knowing the current flowing through the circuit or the charge available, along with the operating voltage [43, 44]. The power consumption of the actuator with the current in the circuit being measured can be calculated as,

$$P_A(t) = V(t)I(t) = V(T)RV_R(t), \tag{2.27}$$

where R is the resistance set at the shunt resistor and V_R is the voltage across the resistor.

The average power consumed can be determined according to,

$$P_A = \frac{1}{T} \int V(t) I(t) dt. \tag{2.28}$$

The capacitor concept is however the more desired method to compute the power consumption by a plasma actuator as the capacitor integrates the current passing through the circuit. This helps in capturing all the micro discharges that happen in time and hence leads to a better signal to noise ratio as compared to the resistor concept.

While using the capacitor in the circuit, it is known that the voltage measured across the capacitor is proportional to the charge across the electrodes of the plasma actuator i.e.,

$$Q(t) = C_P V_P(t). \tag{2.29}$$

The operating voltage and the charge, Q is then plotted against each other in a Q-V cyclogram, commonly known as the Lissajous figure, as proposed by Manley [45]. A typical Q-V cyclogram for a surface discharge plasma actuator is shown in Figure 2.8 taken from Kriegseis *et al.* [46]. Along with power consumption, cold capacitance, C_0, and effective capacitance, C_{eff}, are used to characterize plasma actuators by their electrical properties. Q_{max} and V_{max}, denote the maximum charge and voltage during the actuation cycle, respectively. Cold capacitance is the passive component of actuator capacitance, while the effective capacitance can be defined as the actuator capacitance during the discharge.

The area enclosed in the cyclogram gives the power consumed by the actuator per discharge cycle according to,

$$P_A = \int Q(t) dV(t). \tag{2.30}$$

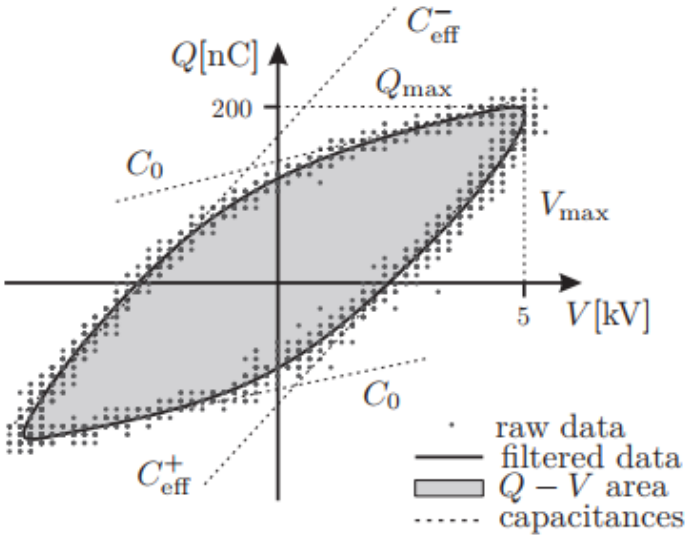

Figure 2.8: Typical Q-V cyclogram of surface DBD plasma actuators with electrical characteristic quantities. Reprinted with permission from Kriegseis *et al.* [46].

In the context of power consumption by a plasma actuator, the power losses happening in an actuation cycle needs to be understood. There are three stages of power losses that takes place in the operating cycle of a plasma actuator. The first one occurs during the conversion of input power to the actuator. The losses occurring during this stage is due to reactive power and dielectric heating. The second stage occurs when the power from the plasma is transmitted to the surrounding air in the form of momentum transfer. The loss at this stage occurs due to the light and sound emission as well as the thermal heating of the surrounding air. The third stage is the power saving. The power losses here are hard to define as the they are mainly dependent on the application [47].

2.11 Operational Trends

The electrical power consumed by the actuator depends on various factors such as the actuator materials, operating voltages and frequencies, actuator geometry as well as other state variables. There has been an effort to find gain a universal relation between the power consumed by the actuator and the operating voltage applied, but due to other factors it is dependent on, this has not been achieved.

Kriegseis *et al.* [48] compared several studies that described the Voltage-Power (V-P) relation of plasma actuators. However, since the studies were conducted at different operational setting and the geometric structures of the actuators were different, only the slope of the curves can be compared. The V-P curves plotted for different studies is shown below in Figure 2.9.

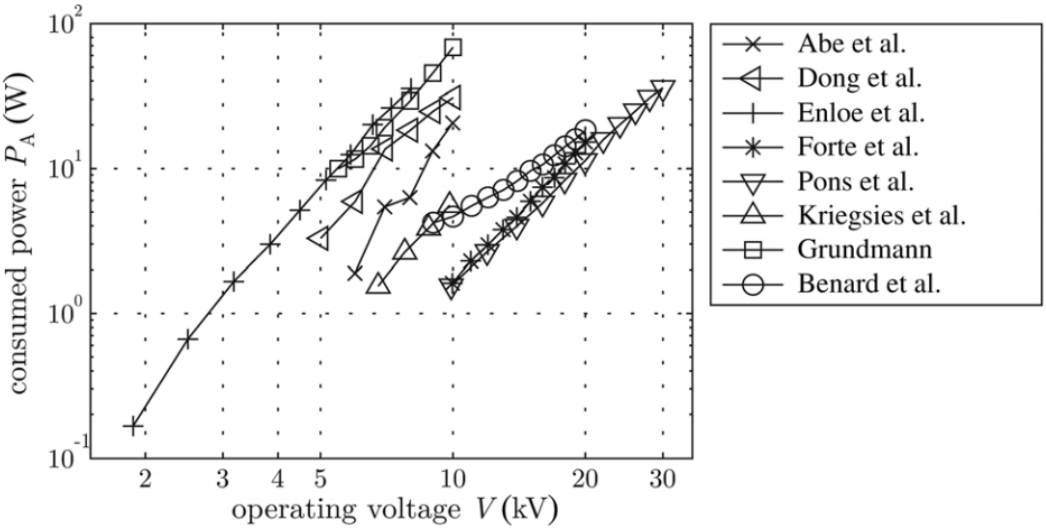

Figure 2.9: Voltage-Power (V-P) relation for various studies reprinted with permission from Kriegseis *et al.* [48].

The voltage power relation has been found to be in the form of P $\propto V_{pp}^{n}$ with some studies suggesting n in the range of $2 < n < 3$ [49, 50]. A number of studies suggested that the value of n was approximately 7/2 [51, 52]. The power frequency relation has been found to be approximately linearly proportional to frequency [53, 13]. For flow control applications, understanding the most efficient way to maximize induced velocity becomes important, which requires better understanding of the force generated by the plasma actuator. This led to the detailed study of the generation and origin of the momentum transfer in a plasma actuator, and effective means to capture the force using flow field measurements described in the present work.

Chapter 3

Experimental Setup

The experiments that were performed for the purpose for this thesis were all complete at the University of Toronto Institute for Aerospace Studies (UTIAS), in collaboration with Dr. Philippe Lavoie of the Flow Control and Experimental Turbulence (FCET) laboratory. The details pertaining to the setup of the experiments and the methods of data acquisition employed are explained within this chapter.

3.1 The Plasma Actuator

The plasma actuator used for each of the experiments was assembled in a conventional way. Based on the literature survey performed, the geometry and materials of the actuator was adopted to maintain a similarity with fundamental work previously done. For example the geometry of the actuator is similar to that of Murphy *et al.* [54]. Self-adhesive copper tapes with thickness of 0.08 mm were used as the electrodes. The actuator was assembled on an acrylic plate. The electrodes and dielectric layers were laid by hand. The actuator length was chosen to be 150 mm. The grounded electrode was placed on the acrylic substrate and wrapped around the side of the plate to ease the electric connections. The electrode had a width of 19.05 mm. The dielectric medium was placed over the grounded electrode. Four layers of Kapton tape each with a thickness of 0.05 mm was used as the dielectric medium.

The schematic for the assembly of the plasma actuator is shown in Figure 3.1. The exposed electrode had a width of 6.35 mm and was placed on top of this dielectric medium, exposed to the air, while being wrapped around the side of the substrate (not visible in Figure 3.1) . There was no gap between the edges of the electrode.

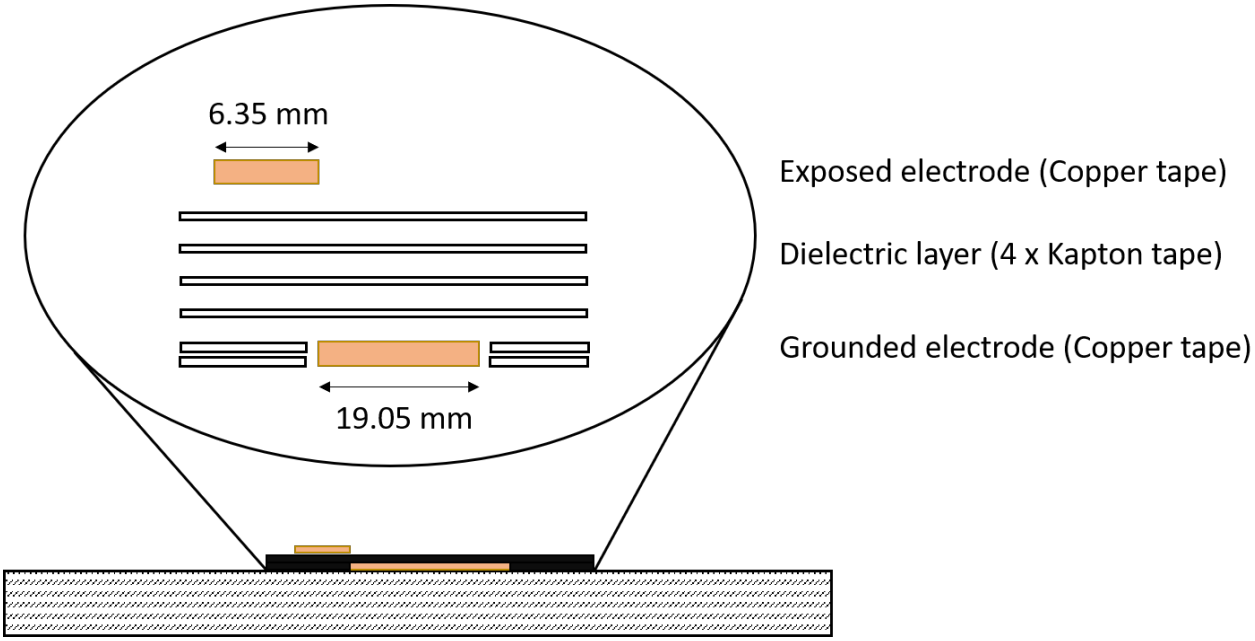

Figure 3.1: Exploded side-view of assembly of the plasma actuator.

The assembly of layers of kapton and copper tapes in a conventional way has its challenges. It is common for imperfections such as wrinkles in the electrodes, or air bubbles between the tape to appear in the process. These imperfections can lead to strong micro-discharges and uneven plasma formation, therefore, care was taken to minimize these imperfections during the assembly. Later the plasma was observed to be approximately uniform, which was sufficient for the purpose of the experiments planned.

The plasma actuators were operated using a high voltage AC signal amplifier, function generator, probe capacitor and a digital oscilloscope. A schematic of the plasma actuator setup used in the current work is presented in Figure 3.2. A Trek Model 20/20c high voltage amplifier was used to supply the voltage to the plasma actuator. The amplifier has a fixed gain of 2000 V/V. It can supply upto 20 kV of peak-to-peak AC voltage. An Agilent 33210A model was used as a function generator to produce sine-waveform signals and set its frequency

and voltage. This function generator was also synced with the PIV system to trigger the image acquisition at specific phases. A digital oscilloscope was used to capture the voltage signal across the probe capacitor (C = 44 nF). Data obtained at specific phases was used for the phase-averaged analysis later discussed in chapter 4 and 5.

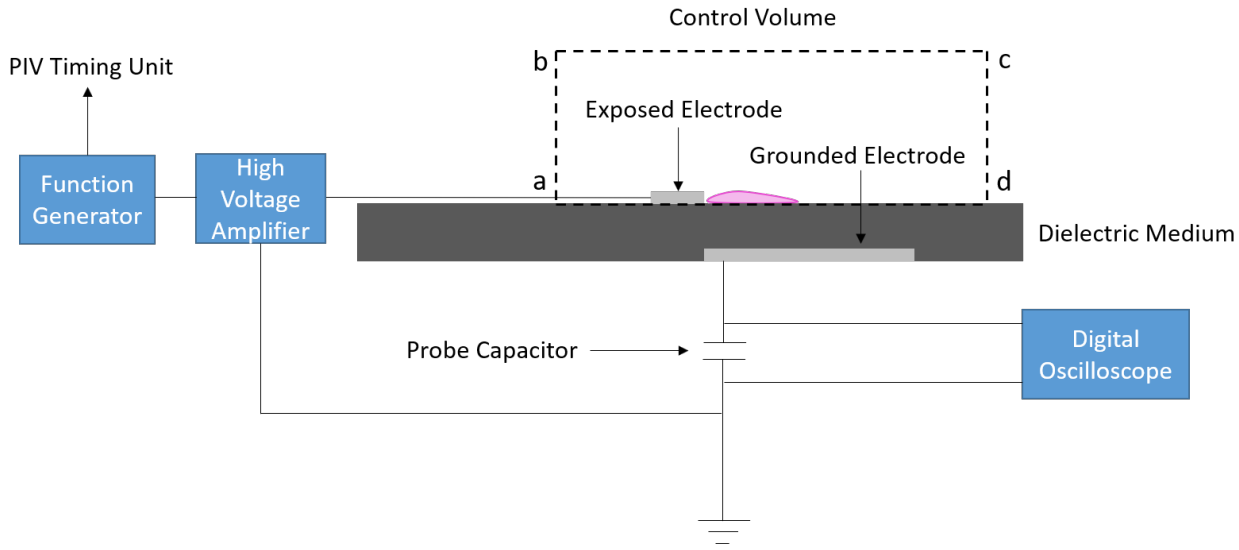

Figure 3.2: Schematic of a DBD plasma actuator setup.

A probe capacitor is generally used to measure power consumed by the actuator. However, no power measurements were performed for the current study. For further reading, Kriegseis *et al.* [46] and Hanson *et al.* [55], provide a comprehensive overview of the power measurement setup for plasma actuators.

3.2 Particle Image Velocimetry

To study the flow behaviour and the acceleration in the flow, Particle Image Velocimetry (PIV) measurements were performed near the plasma-forming region of the actuator. Velocity fields were collected for various operating voltages, V = 7-9 kV at frequencies, f = 1-3 kHz to investigate the effect of these parameters on the resulting body force of the plasma actuator, and also study the spatial and temporal evolution of body force. Increase in volt-

age in order of kilo-volts resulted in a significant increase in induced velocity. Past studies have shown the trend to be non-linear [52, 50, 54].

The schematic of the experimental setup is shown in Figure 3.3. The actuator was placed in an acrylic enclosure (500 x 500 x 500 mm^3) to provide optical access for the camera and the laser-light sheet. The plasma actuator length was 150 mm. Compared to which the quiescent chamber was large therefore no wall effects is expected. The plasma actuator was placed on a 4 degree of freedom (3 translational and 1 rotational degree of freedom) stage, to adjust the position of the plasma actuator within the field of view (FOV) of the camera. The plasma actuator on the positioning stage was set flat within +/- 0.5 deg using an inclinometer.

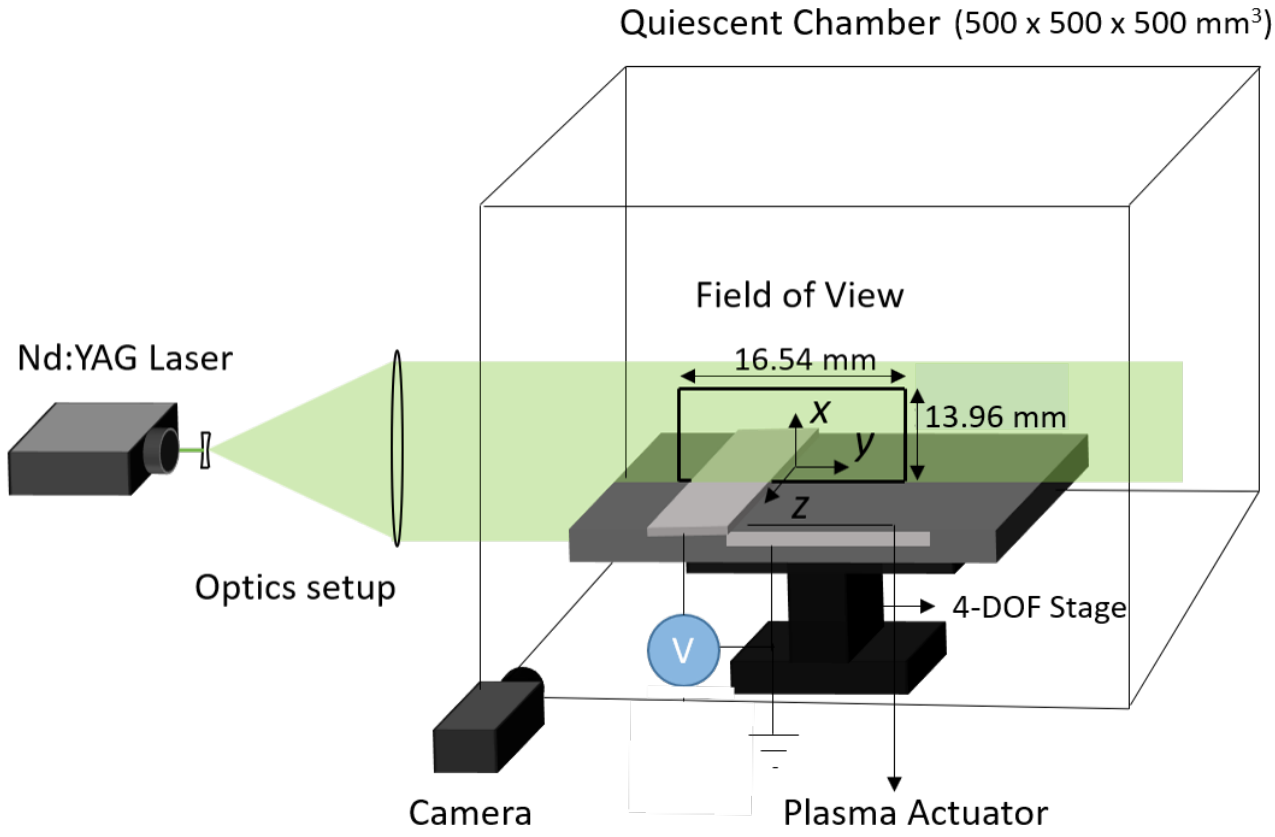

Figure 3.3: The arrangement of the components of the PIV system including the laser sheet, camera and chamber for testing.

A 2D PIV system from LaVision was used for the current work. The system consisted of the Evergreen Nd:YAG laser system, emitting a laser of wavelength 532 nm and pulse energy of 200 mJ. The laser was used to illuminate the particles in the quiescent chamber containing the plasma actuator. The chamber was filled with particles ($\approx 1\mu$m) from an in-house seeder using Di-Ethyl-Hexyl-Sebacat (DEHS) oil. The flow induced during seeding is allowed to become still before acquiring data. The camera used with this PIV system is an Imager sCMOS camera with a resolution of 2560 x 2160 pixels. The camera had a Tamron 180 mm lens which was used to achieve a FOV of 16.54 x 13.96 mm at a working distance of 500 mm.

3.2.1 Calibration plate

The small ROI being considered in this work required the use of a custom made calibration target to to provide a minimum of 20 calibration points over the field of view to convert from pixel space to geometric coordinates. A sheet of printed circular dots was pasted onto a flat metal plate to be used as the target. Each circular dot on the target had a diameter of 0.7 mm and the dots were spaced 2 mm apart. Calibration from pixels to physical space in units of millimeters was performed as a step within the Davis software.

3.2.2 Laser Sheet

Two lenses were used to convert the laser beam to a focused, thin, rectangular laser sheet. A schematic of the lens setup used in the current work is showin in Figure 3.4. The laser beam is initially passed through an Iris, to remove the outer radiation or reflections around the beam. It is then passed through diverging lens with radius 13.1 mm that spreads the beam into a diverging laser sheet. The laser sheet has a Gaussian distribution of intensity. Passing this through a spherical lens, changes the laser sheet to a rectangular form thereby increasing the width of the intensity distribution. A similar optical setup was used by Naguib-Lahouti *et al.* [5] and Houser [11] in their work.

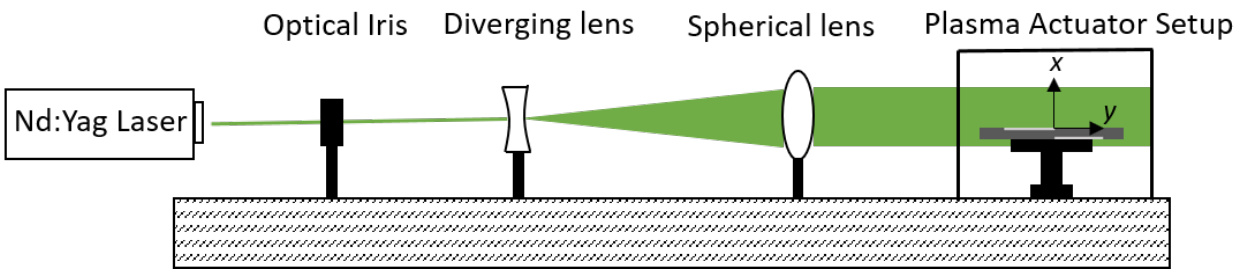

Figure 3.4: Schematic of optical setup for PIV.

3.3 Particle Image Velocimetry Data Acquisition

There are primarily two ways to acquire images during PIV, based on the instance at which the images are recorded, and averaged. The concept of ensemble averaging and phase reference are the key to understand these two methods of acquiring PIV data. Ensemble averaging, by definition, in the present context refers to averaging the data collected at a particular time instance. The concept of phase reference can be defined as the process where a trigger can be set to acquire data at given time intervals along the actuation cycle. Of the two methods, the first one namely, *Time-averaged* measurements, is where the images are captured over a period of time, irrespective of the phase of actuation signal, and are averaged to study the flow field. This method of averaging over a period of time is useful in studying flows that are statistically steady. The second, is by means of *Phase Averaged* measurements. For this technique the images are captured at specific phases of actuation or forcing. The images captured are ensemble averaged at the specific phase to study the flow field at a particular instance of actuation cycle. This data helps in understanding the development of the flow within an actuation cycle. However, phase averaging allows use of a slower system, as used in the present study, to capture variation of flow if and only if the flow is cyclic in nature, i.e. has an clear underlying periodic variation. The cyclic nature of the flow would mean that the phase data can be acquired over a large number of cycles and then averaged to study the flow in the given phase of actuation cycle. If the flow is not cyclic, a much faster data acquisition system would be required to capture all the data within one cycle of actuation.

In this work, the plasma actuator was operated at very high frequencies (1-3 kHz). An effort was made to resolve the sinusoidal voltage used to actuate the plasma actuator into 8, 16 and 32 phases. Each of these phases correspond to an an instance in time. Since, the working principle of PIV involves capturing two images and the correlating the motion of particles, it becomes impossible to capture two images to correlate at the same time. Therefore, to capture the forcing at time t, the system is calibrated to capture an image at $t + \Delta t$ and t - Δt. Correlating these images gives the best approximation of the flow field at time, t. The Δt is maintained to be as small as possible. In this work, Δt is determined by the looking at the amount of particle displacement between the two images. The fact that the particle displacement would be different for the range of operating voltages and frequencies was noted, and therefore the Δt was calculated separately for a certain operating condition.

For visualisation purposes, this method is depicted in Figure 3.5 below. For example, to analyse the flow field at phase angle of $\pi/2$, occurring at an instance t, the images are acquired at the instances 1 and 2 (depicted by the orange lines), Δt apart from t. This process in carried out for all the required phases in the actuation signal. The time between the two phases in the actuation cycle is given by the term, ∂t .

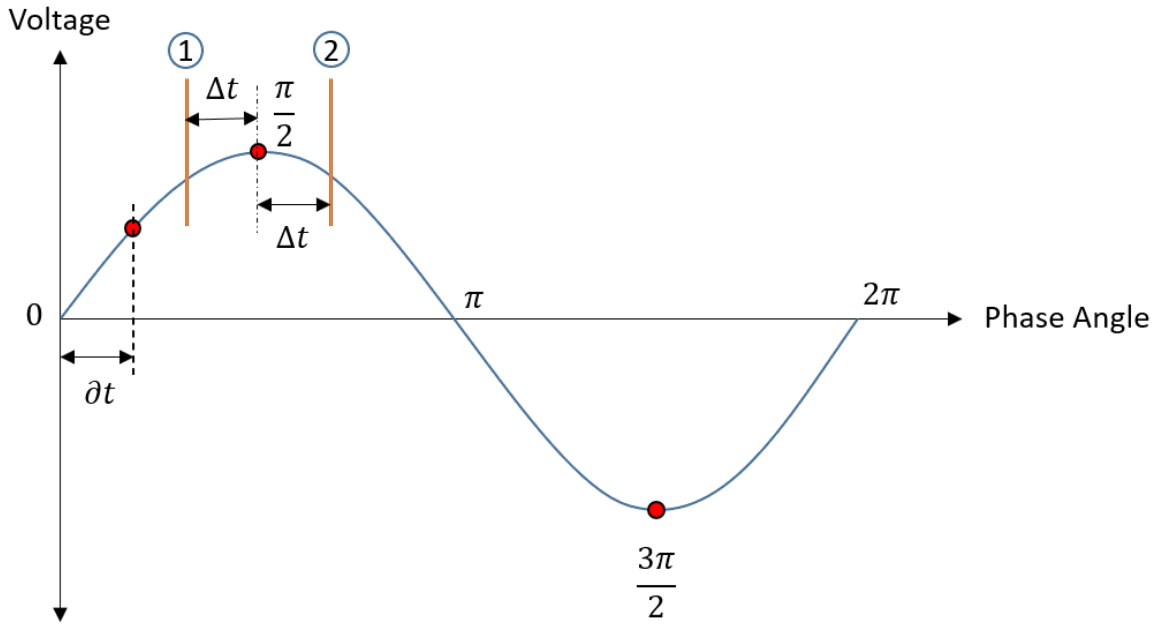

Figure 3.5: Description of the timing of the image pairs for the PIV analysis.

A summary of the dataset acquired using PIV for the present work is provided in Table 3.1. The first column contains the different frequencies the actuator was operated at. The second column contains the different applied voltages to the actuator for the given actuator frequency. In the third column, the number of phases at which data was acquired for a combination of frequency and voltage given in the row, is shown.

Table 3.1: Summary of experimental dataset for PIV measurements.

Frequency	**Voltage**	**Data Acquired**	**Time between phases**
3 kHz	7 kV, 8 kV, 9kV	8 phases and 16 phases	41.66 μs and 20.83 μs, resp.
2 kHz	7 kV, 8 kV, 9kV	8 phases and 16 phases	62.5 μs and 31.25 μs, resp.
1 kHz	8 kV, 9kV	32 phases	31.25 μs

3.4 Particle Image Velocimetry Data Preprocessing

The initial processing of the data was performed using the same commercial Software (Davis 8). The raw images were at first passed through a subtract-sliding average filter to eliminate background noise. Then a geometric mask was used to omit the region outside the region of interest. Sequential cross-correlation of the images was performed. A decreasing multi-pass processing window function was then applied withing the region of interest, with 50% window overlap. In the first pass, square shaped processing window with dimensions of 32 x 32 pixels is used, and in the second pass, circular window is chosen with the reduced size of 8 x 8 pixels. No vectors were filled, and the spurious vectors were approximated manually through Matlab, as described in Section 3.5. The standard deviation of the velocity fields was observed to check and eliminate images pairs with high noise regions inside the Region of Interest (ROI).

The field of view as captured by the PIV camera is shown in Figure 3.6. The seeding used in PIV measurements can be seen in the upper half of the figure. The downstream edge of the exposed electrode was chosen to be the origin (x = y = 0) in the measurement plane and is denoted by a red dot in the figure. The processing was done in the ROI (enclosed in blue) with the dimensions of 11.65 x 2.97 mm, as shown in Figure 3.6. The coordinates of the left-bottom corner of the ROI is (x = -1.68 mm, y = 0 mm). This region is chosen as the ROI as it captures the accelerating flow, studying which is one of the objectives of the present work. This ROI contained 452 x 116 vectors with the spatial resolution (spacing between the vectors) of 0.0259 mm, in both directions. The electrodes of the plasma actuators are shown in white, and the orange line encloses the region of plasma formed. The direction of the flow is from the left side to the right of the image.

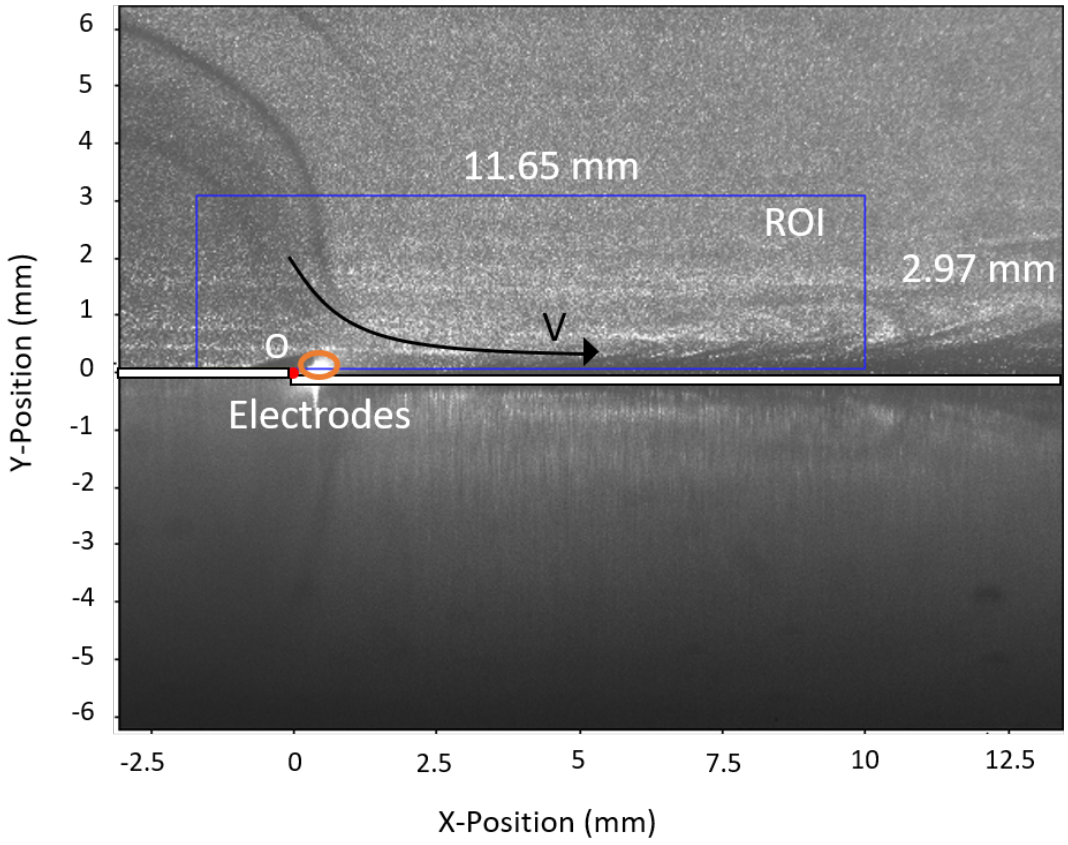

Figure 3.6: Field of View from the PIV camera, depicting the ROI.

3.5 Data Processing on Matlab

Velocity field data that was calculated from the image pairs using the Davis software was exported to Matlab for further post-processing. For each set of data, i.e. at each phase, a total of 250 processed velocity fields were exported. The data was sorted into three-dimensional matricies for dimensions m by n by z. The first two dimensions of m and n correspond to the two-dimensional plane of the planar PIV data, whereas the third coordinate corresponds to the index of the particular instantaneous velocity field. For each of the velocity fields a two-dimensional (2D) Gaussian filter was applied. Applying a Guassian 2D filter is common practice with respect to PIV data, and can be applied within the Davis program, however, in the present work this step was done within Matlab to have more scrutiny over the data. The Gaussian filter was defined such that the data was ideally smoothed and filtered in the direction that is parallel to the wall, where the actuator was located. It was applied to a region of 5 by 3 cells with a standard deviation of 1.7 using the function *fspecial* in Matlab. To further eliminate the spurious vectors a two step process was implemented as described below.

- **Step 1:** Consider an arbitrary cell, (m, n), in the data field. The standard deviation of the cells along z was calculated, where z represents the number of the image in the 3D matrix, m x n x z, as shown in Figure 3.7. If the value of the cell was beyond the standard deviations of 1.5 from the mean value along all z, then it was replaced by the mean of the values of (m, n) along z-direction, for better approximation. The standard deviation of 1.5 was chosen since it corresponds with 43.3% confidence window across the mean value.

- **Step 2:** The value of the surrounding cells of (m, n) in the given z plane is considered. If the value of (m, n) is outside the limits of one standard deviation of values of its surrounding cells, the (m, n) is replaced by the mean mean value of the adjacent 8 cells.

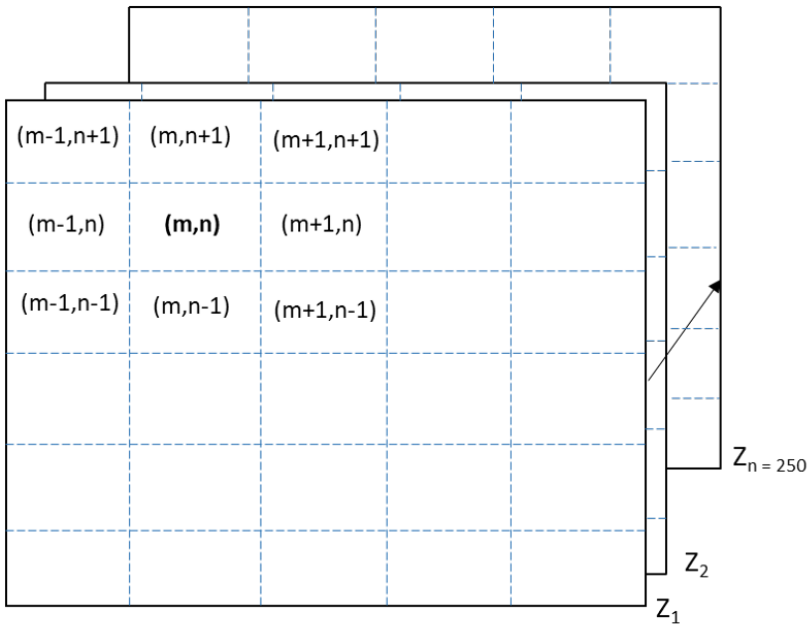

Figure 3.7: Representation of data processing in Matlab.

Since the values at the end of Step 1, are dependent on the values of (m, n) along the z-direction, they could be an aberration in the given plane. To reduce or eliminate these aberrations, Step 2 is followed, so that the values are not only a good average of all 250 images, but also in bounds of cells surrounding them in the given plane.

Chapter 4

Phase Resolved Body Force Results

4.1 Overview

Plasma actuators are used to transfer momentum to the surrounding air. In a quiescent chamber the plasma actuator generates a wall jet. In the first section, the flow generated by the actuator is examined and compared with theoretical observations made in previous studies. Along with the evolution of the body force within the voltage cycle of the actuator, the spatial distribution of the electrohydrodynamic force averaged over several cycles was also investigated. The spatial and temporal evolution of the local acceleration term in the momentum equations is emphasised. In the final section, the effect of the operating conditions on the spatial distribution of the force was examined. The 16 phase data acquired at various operating conditions was used to study the momentum transfer, presented in this chapter. The experimental setup and methodology relevant to this research is presented in Section 3.2.

4.2 Flow Induced by the Plasma Actuator

Glauert [28] provides the analytical solution for a laminar wall jet as discussed in Section 2.4. The velocity profiles of a wall jet are conventionally characterized by the magnitude of maximum velocity, U_{max}, and the half jet width, $\delta_{1/2}$. The half jet width is used as a

normalization factor to scale the theoretical profile, and is defined as the location above the peak velocity where the velocity profile reaches half the maximum velocity,

$$\delta_{1/2} = y(\frac{U_{max}}{2}). \tag{4.1}$$

The Glauert profile for the laminar wall jet is shown in Figure 4.1, along with the velocity profiles at $x = 2$ mm, 4 mm and 6 mm downstream of the trailing edge of the exposed electrode. The velocity profiles are acquired by averaging velocity fields of 16 phases within the actuation cycle, for a flow field generated when the actuator was operated at a voltage of 8 kV and frequency of 3 kHz. The standard wall jet similarity scaling is adopted, where the U component of the velocity is normalized by the maximum velocity at the respective x-location, $U_{max,x}$, and the wall normal distance, y, was normalized by $\delta_{1/2,x}$, which can be depicted as,

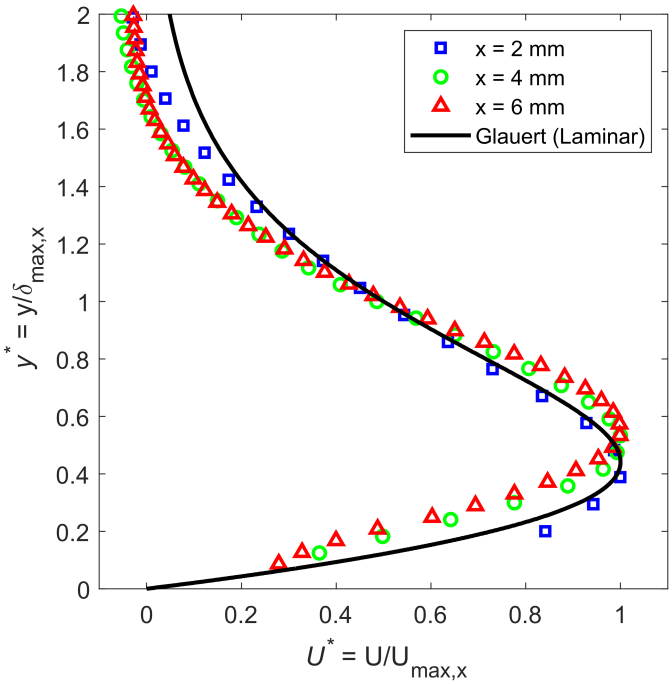

Figure 4.1: Normalized velocity profiles at $x = 2$, 4 and 6 mm, of flow induced by actuator operated at $V = 8$ kV, $f = 3$ kHz.

$$y^* = \frac{y}{\delta_{1/2,x}}, \quad U^* = \frac{U}{U_{max,x}}. \tag{4.2}$$

Results show that the velocity profiles, normalized according to Equation 4.2, at various downstream distances closely resembles the laminar wall jet profile of Glauert [28], as seen in Figure 4.1. Previous studies [56, 54], have normalized the theoretical velocity profiles similarly, based on Glauert's solution, and it was observed that the maximum velocity is located at $y^* \approx 0.5$, for laminar wall jets and $y^* \approx 0.25$, for turbulent wall jets. It is

observed for the velocity profiles shown in Figure 4.1, the maximum velocity is located at $y^* \approx 0.5$, suggesting that the wall jet being studied in the present work is laminar.

Schwarz *et al.* [57] and Glauert [28], noted that theoretically, for a laminar wall jet the maximum velocity decreases with the downstream distance proportional to, $U_m \propto x^{-0.5}$, and that the half jet width increased with the downstream distance in accordance with, $\delta_{1/2} \propto x^{0.75}$. The variation of the maximum velocity and the half jet width along the downstream distance, was expected to be exponential based on the aforementioned theoretical studies. Figure 4.2 (a) and (b), show the variation of the maximum velocity and the half jet width downstream of the trailing edge of the exposed electrode, respectively. The data is plotted on logarithmic scales to better visualise the exponential variation.

A best-fit line to the data is also plotted in order to obtain the exponential factor. The data points at $x = 1$ mm and 2 mm, have been excluded from the linear fit due to their vicinity to the discharge. It was observed that the maximum velocity was proportional to $x^{-0.46}$ and the half jet width was seen to be varying proportionally to $x^{0.81}$, where x is the downstream distance from the plasma actuator. The negative exponential factor signifies the decay of the maximum velocity, due to the shear force. The increase in the half jet width can be attributed to the law of conservation of momentum, as the two-dimensional jet widens when the velocity reduces.

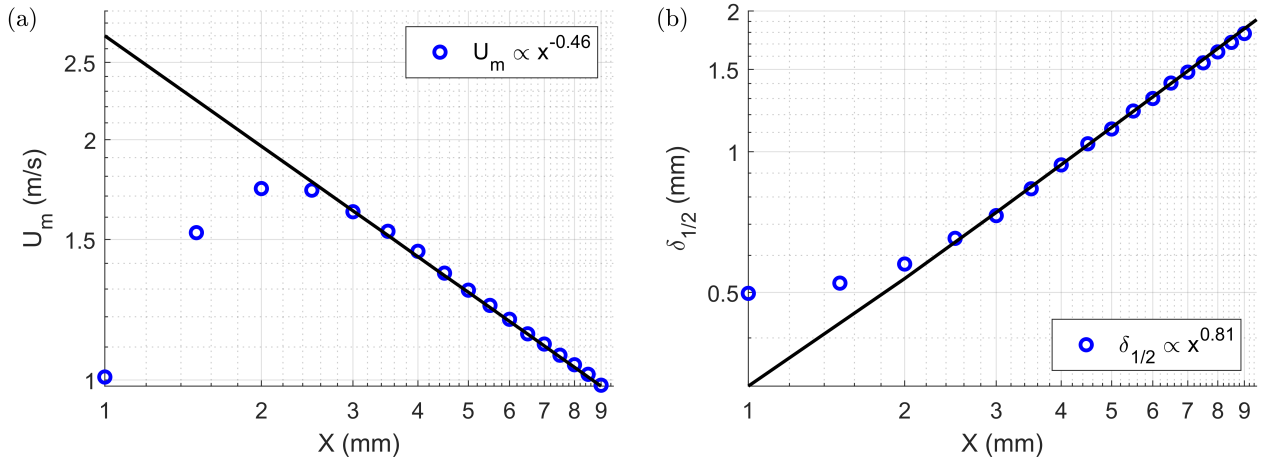

Figure 4.2: Variation of (a) maximum velocity, U_{max}, and (b) half-jet width, $\delta_{1/2}$, along downstream distance, x; $V = 8$ kV, $f = 3$ kHz.

4.3 Body Force

Considering the wall jet generated by the plasma actuator to be a two-dimension and incompressible flow, rearranged momentum equations are used in their discrete form to obtain the spatial and temporal distribution of the electrohydrodynamic force per unit volume:

$$f_x(x,t) = \underset{(1)}{\frac{\partial p(x)}{\partial x}} + \underset{(2)}{\rho\frac{\partial U_x(x,t)}{\partial t}} + \underset{(3)}{\rho\left(U_x(x,t)\frac{\partial U_x(x,t)}{\partial x} + U_y(x,t)\frac{\partial U_x(x,t)}{\partial y}\right)} - \underset{(4)}{\mu\left(\frac{\partial^2 U_x(x,t)}{\partial x^2} + \frac{\partial^2 U_x(x,t)}{\partial y^2}\right)}, \tag{4.3}$$

$$f_y(x,t) = \underset{(1)}{\frac{\partial p(x)}{\partial y}} + \underset{(2)}{\rho\frac{\partial U_y(x,t)}{\partial t}} + \underset{(3)}{\rho\left(U_x(x,t)\frac{\partial U_y(x,t)}{\partial x} + U_y(x,t)\frac{\partial U_y(x,t)}{\partial y}\right)} - \underset{(4)}{\mu\left(\frac{\partial^2 U_y(x,t)}{\partial x^2} + \frac{\partial^2 U_y(x,t)}{\partial y^2}\right)}, \tag{4.4}$$

where, f_x and f_y are the x- and y-components of the volume force, respectively (refer Fig.3.6). The term p is the pressure acting on the fluid, whereas ρ and μ represent the density and dynamic viscosity of the fluid, respectively. The velocity components in the Cartesian space are given by U_x and U_y. The term ∂t is the time between the two considered phases in the actuation cycle (refer Fig.3.5). It is calculated by dividing the time period of the actuation cycle by the number of phases it is discretized into. The first term on the right hand side of Equations 4.3 and 4.4 is the *pressure term*, which has been assumed to be insignificant in the present work based on previous studies mentioned in Section 2.6. The second and third terms known as the *local acceleration term* and the *convective term*, respectively, provide the spatial distribution of the local acceleration and the convective force, at a time instant, t. The fourth term, known as the *viscous term*, signifies the contribution of the viscous forces to the total volume force. The value of density was chosen to be 1.225 kg/m^3 and that of

dynamic viscosity was chosen to be 1.81 x 10^{-5} kg/m.s, assuming the initial conditions of 1 atm pressure and 15° C.

The first-order and second-order derivatives in the Equations 4.3 and 4.4 were calculated by applying the second-order central differencing schemes. The body force components F_x and F_y is then computed by integrating the volume force, $f_{x,y}$ over the surface, S, which covers the region of interest, according to,

$$F_x(t) = \iint_S f_x(x, y, t)\, \mathrm{d}x\mathrm{d}y, \tag{4.5}$$

$$F_y(t) = \iint_S f_y(x, y, t)\, \mathrm{d}x\mathrm{d}y. \tag{4.6}$$

The variation of the horizontal component of body force, F_x, along the phase angle is shown in Figure 4.3. The values were obtained at an operating voltage of 9 kV and actuation frequency of 3 kHz. The peak-to-peak voltage is shown along the right axis of the figure, while F_x is shown along its left axis. It must be noted that the plots are repeated twice in the figure for better visualisation.

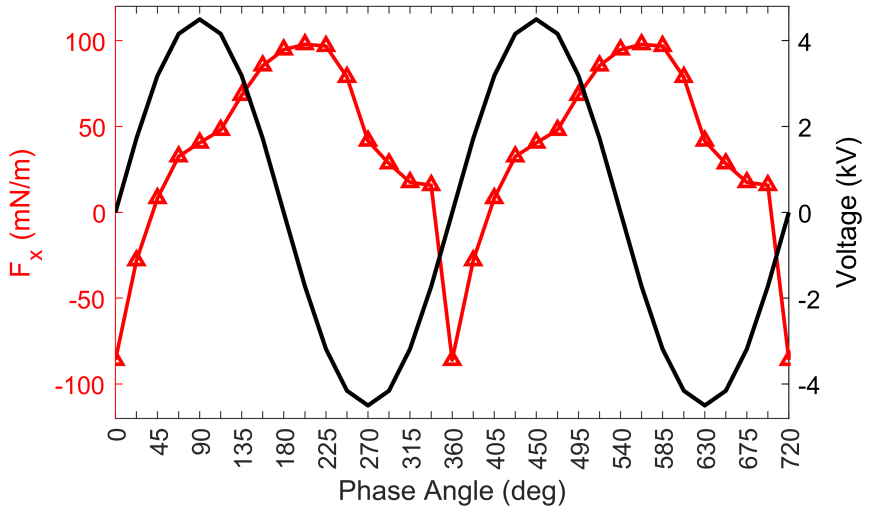

Figure 4.3: Phase-averaged values of the horizontal component of body force, F_x at $V_{pp} = 9$ kV and $f = 3$ kHz.

The behaviour of the body force is observed to be similar to the previous work, as discussed in Section 2.2. The body force is seen to peak in the negative half-cycle of actuation and is the lowest in the positive half-cycle. The body force is found to vary from a negative value in the positive half-cycle to a positive value suggesting a change in the direction of the force, similar to observations made by Porter *et al.* [13] and Font [14].

The magnitude of the induced velocity varies throughout the actuation cycle of the plasma actuator. The variation of maximum induced velocity in the x-direction, U_{max} is shown in Figure 4.4. For the given operating conditions, it can be seen that the maximum value of induced velocity occurs at phase angle, $\phi = 315°$. This trend suggests that the maximum induced velocity occurs in the negative half-cycle, when the exposed electrode is negatively charged. It has been previously observed that in this half of the actuation cycle, the maximum velocity is primarily induced by the exposed electrode as negative ions are the main contributors to the momentum transfer [58]. On the contrary, the induced velocity is at its lowest during the positive half cycle, when the velocity is primarily induced by the grounded electrode. The magnitude of the velocity induced by the grounded electrode is lower than when induced by the exposed electrode because, it is separated from the fluid by the dielectric medium.

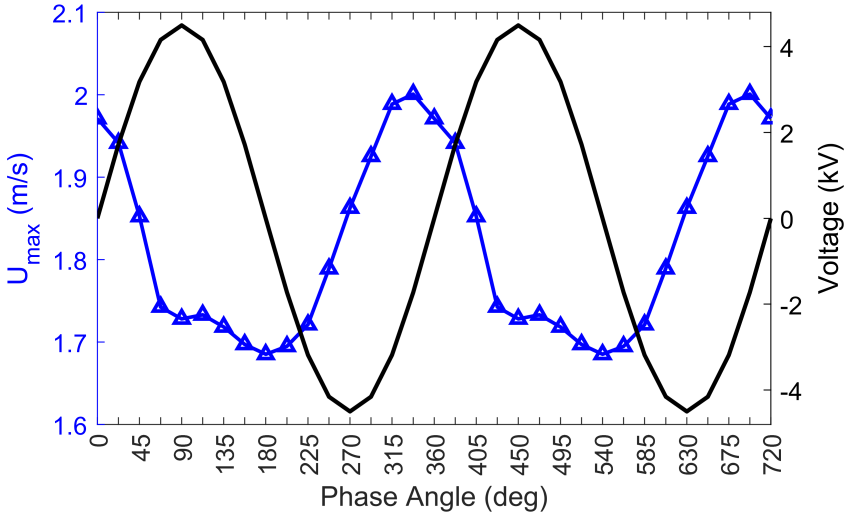

Figure 4.4: Phase averaged values of the horizontal component of the maximum induced velocity, U_{max} at $V_{pp} = 9$ kV and $f = 3$ kHz.

The location of the maximum induced velocity is also dependent on the phase angle of actuation. The variation of location of maximum induced velocity, from the downstream edge of the exposed electrode, $x(U_{max})$, is shown in Figure 4.5. The general trend as seen in the figure, suggests that the location of maximum induced velocity is closer to the downstream edge of the exposed electrode during the negative half-cycle and further downstream of the electrode during the positive half-cycle.

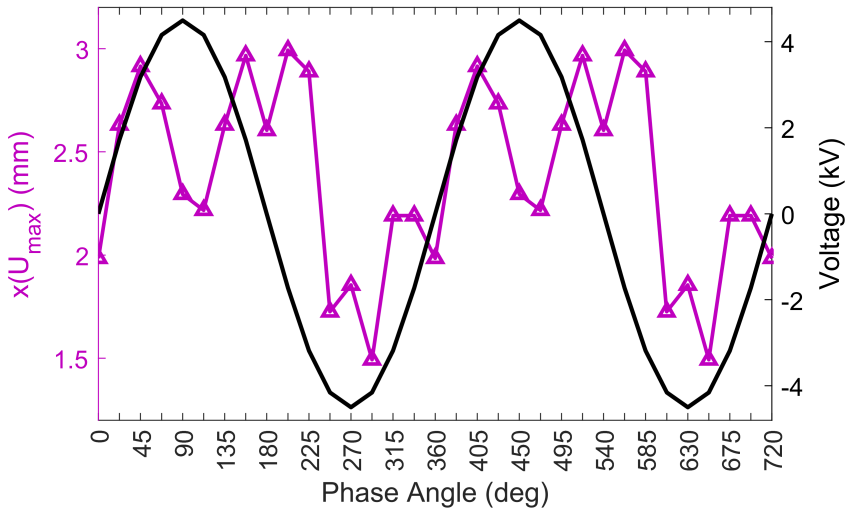

Figure 4.5: Location of the horizontal component of the maximum induced velocity from the downstream edge of the exposed electrode, $x(U_{max})$ at $V_{pp} = 9$ kV and $f = 3$ kHz.

4.4 Velocity Fields

The velocity fields of the x-component of velocity, U_x, around the plasma actuators, within the ROI (shown in Fig.3.6) is obtained from PIV measurements when the actuator was operated at a voltage of 9 kV and frequency of 3 kHz is shown in Figure 4.6. The evolution of the velocity fields at 8 phases in the actuation cycle, is shown through Figure 4.6(a) to (h). The maximum induced was found to be at phase angle, $\phi = 315°$ and the minimum was at phase angle, $\phi = 180°$. These contours depict the unsteady nature of the flow generated by the plasma actuator within an actuation cycle.

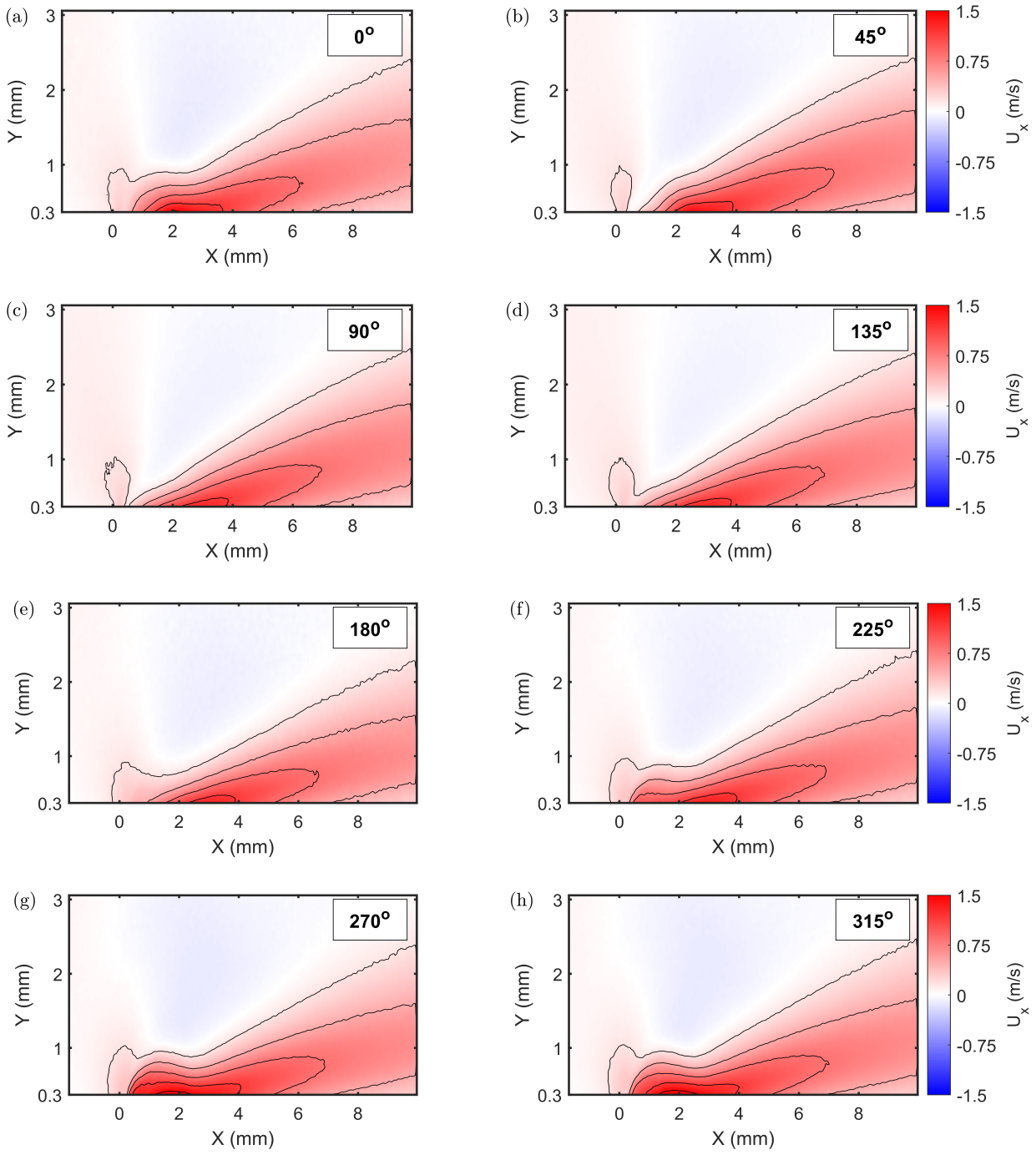

Figure 4.6: Velocity contours of the x-component of velocity, U, at $V_{pp} = 9$ kV and $f = 3$ kHz. Contour spacing of lines plotted, 0.33 m/s.

4.5 Evolution of the Body Force

The body force computed using Equations 4.3 and 4.4 has contributions from each term of the equations and in this section the relative contribution of the terms are considered. In Figure 4.7, the variation of the horizontal component of body force, F_x, and the terms of the momentum equations over an actuation cycle is shown. The data shown was acquired for flow induced by the actuator operating at a voltage of 9 kV and frequency of 3 kHz. The total horizontal force, F_x and the local acceleration term are plotted along left axis and the convective and viscous terms are plotted along the right axis. The black curve is representative of the applied voltage.

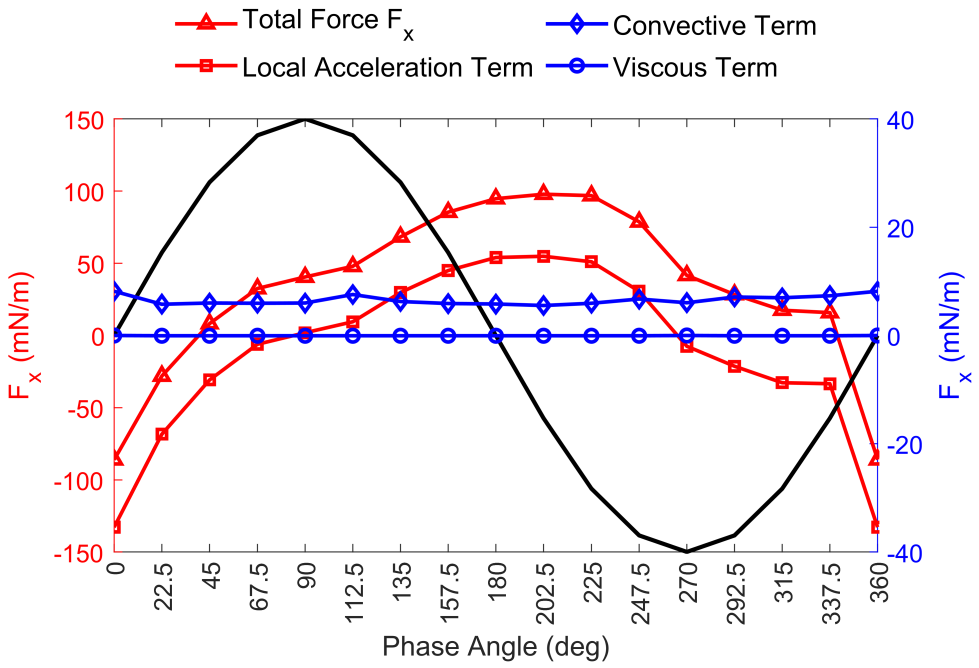

Figure 4.7: Time evolution of the horizontal component of body force, F_x, calculated using Equation 4.5, and separate contribution of each of the terms of Equation 4.3, for $V_{pp} = 9$ kV and $f = 3$ kHz.

Over a complete cycle of actuation, the force production by the actuator is known to be unsteady in nature [5, 39]. It is shown in Figure 4.7 that the local acceleration term has a major contribution to the body force within a cycle of actuation. On comparing the RMS values of each of the components, it was found that the RMS value of local acceleration

term was 89.6% the RMS value of total unsteady force production. The convective term is observed to hold a near constant value throughout the cycle of actuation ($\approx$ 10 mN/m). The contribution of the viscous term indicates that the viscosity within the flow field is comparatively very low, and is nearly constant similar to the convective term. The contribution of the local acceleration term to the body force is seen to be constantly higher in absolute magnitude than that of the other terms.

4.6 Spatial Distribution of the Force

While the force produced by the actuator varies with respect to the phase of the applied voltage waveform, when averaged over the complete cycle a mean value may be calculated. In many flow control experiments, the mean (effectively quasi-steady) value is of interest [17]. The spatial distribution of volume force and the contribution of all the terms in x- and y-directions are calculated using Equations (4.3) and (4.4), respectively. The x- and y-components of the total force and the constituent terms were then averaged over all 16 phases, and is shown for in Figure 4.8 and 4.9, respectively, similar to Benard *et al.* [17]. The mean force components are $\langle f_x \rangle$ and $\langle f_y \rangle$, where $\langle\ \rangle$ denotes average over phases. The mean horizontal component of the force, $\langle f_x \rangle$, is seen to be positive in the region of discharge ($\approx$ 4000 N/m^3) and a small negative region of the force is observed downstream of the discharge, as seen in Figure 4.8(a).

It can be observed that the local acceleration term, as is shown in Figure 4.6(b), does not contribute to the mean horizontal force, referred to as the total mean force in Figure 4.8(a), when averaged over several cycles of actuation. This is because the flow accelerates and decelerates in a similar form over one cycle, which leads to flow being quasi-steady when averaged over several actuation cycles. spatial distribution and magnitude of the convective term as shown in Figure 4.8(c) appears to be the most significant contributor to the total mean force shown in Figure 4.8(a). The convective term comprises nearly 96% of the total mean force in the x-direction and thus these plots appear similar. A negative region, downstream of the discharge is also observed in the spatial distribution of the convective

forcing term in Figure 4.8(c). A similar negative region can also be seen downstream in the spatial distribution of the convective term depicted in Benard *et al.* [17]. The viscous term has a much lesser contribution as compared to the other terms. It can be seen seen in Figure 4.8(d), that its effect on the scale is nearly null. The contribution of the local acceleration term and the viscous term is sufficiently small in Figures 4.8(b) and (d), respectively, such that it appears white.

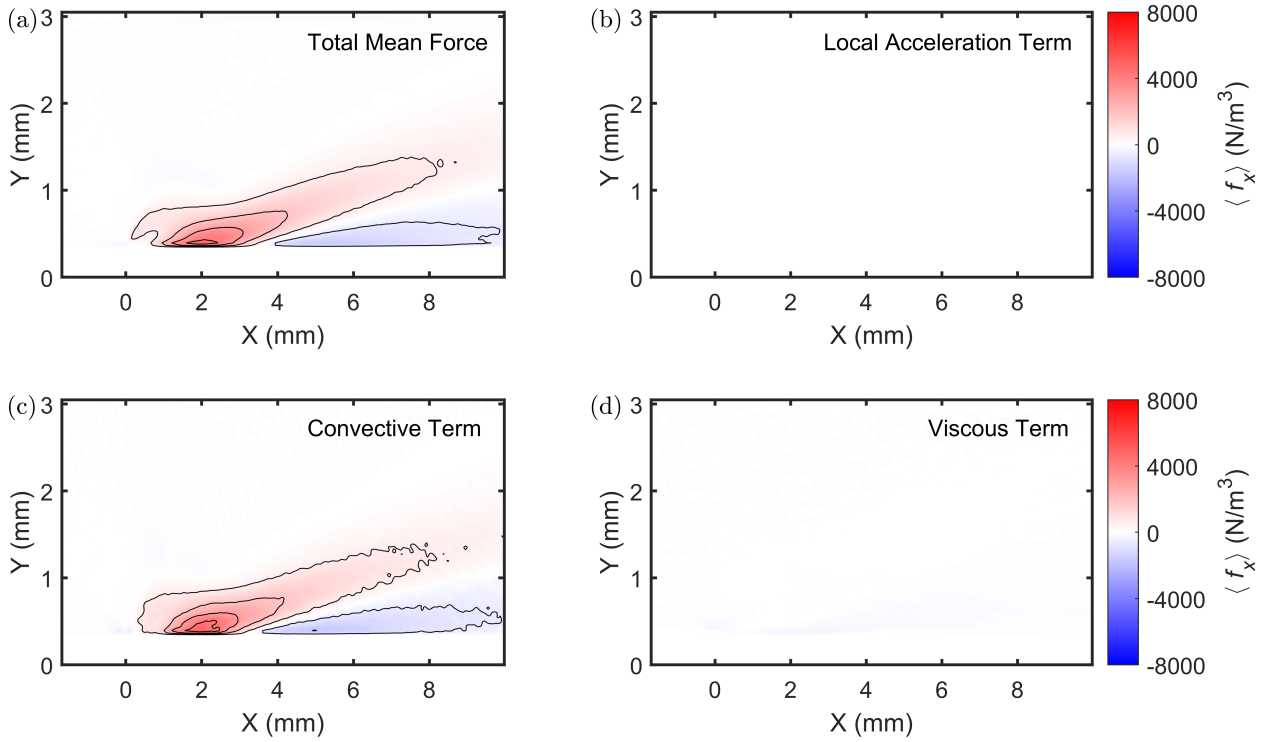

Figure 4.8: Spatial distribution of (a) the total mean force, $\langle f_x \rangle$, (b) the local acceleration term, (c) the convective term, (d) the viscous contribution in the x-direction determined according to Equation 4.3. Location of the edge of the exposed electrode, (x = 0, y= 0). $V_{pp} = 9$ kV and $f = 3$ kHz. Contour spacing of lines plotted, 1230.8 N/m^3.

However, it is possible that the viscous term has a significant value between $y = 0$ mm and $y = 0.3$ mm, which has been omitted in the current analysis. Nevertheless, previous studies [17, 48] have suggested that the value of viscous term would still be insignificant while compared to the contribution of the other terms, as major part of the momentum transfer occurs outside the boundary layer region.

Similarly, the spatial distribution of the vertical component of the mean force, $\langle f_y \rangle$ and the terms contributing to it was calculated using the Equation 4.4. Figure 4.9(a) shows the spatial distribution of the y-component of the mean force. The value of this force component as compared to the primary mean force component shown in Figure 4.8(a), is significantly less. The integrated total force x-direction constituted 97.1% of the total force as compared to 2.9% in the y-direction. Thereby, these plots further confirm that the forcing is highly uni-directional, i.e. $\langle f_x \rangle \gg \langle f_y \rangle$.

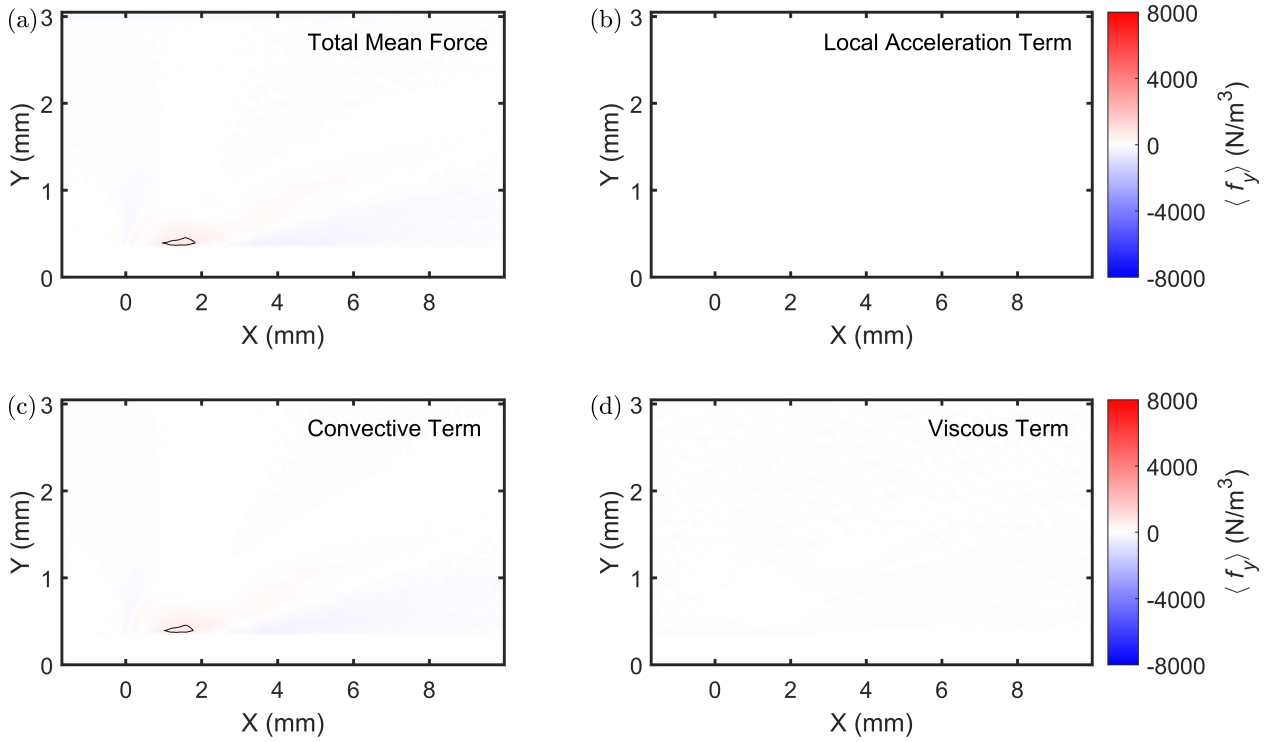

Figure 4.9: Spatial distribution of (a) the total mean force, $\langle f_y \rangle$, (b) the local acceleration term, (c) the convective term, (d) the viscous contribution in the y-direction determined according to Equation 4.4. $V_{pp} = 9$ kV and $f = 3$ kHz.

The contribution of the local acceleration term, shown in Figure 4.9(b), is insignificant as the force component along the y-direction is very small. The contribution of the viscous term, depicted in Figure 4.9(d), is nearly non-existent. The convective term distribution, shown in Figure 4.9(c) however, is still seen to be the major contributor for this component of the mean force. In the present work, for the given operating conditions, the convective term was observed to contribute up to 96% of the y-component of mean force, $\langle f_y \rangle$.

4.7 Temporal and Spatial Evolution of the Local Acceleration Term

In Section 4.4, it was observed that the local acceleration term is the major contributor to the total body force, F_x. The spatial distribution of the local acceleration term over the actuation cycle is studied this section. The data were acquired at 16 phases within the actuation cycle of the plasma actuator operating at a voltage of 9 kV and frequency of 3 kHz. Figure 4.10 depicts the phases at which the data was acquired along the applied voltage curve. In order to better understand the temporal evolution of the local acceleration through the actuation cycle, the cycle is divided in to the negative-going cycle and the positive-going cycle. The phase angles in the negative-going cycle ($\phi = 90°$ to $247.5°$) is depicted with blue, and the positive going cycle ($\phi = 270°$ to $67.5°$) is depicted in red in Figure 4.10.

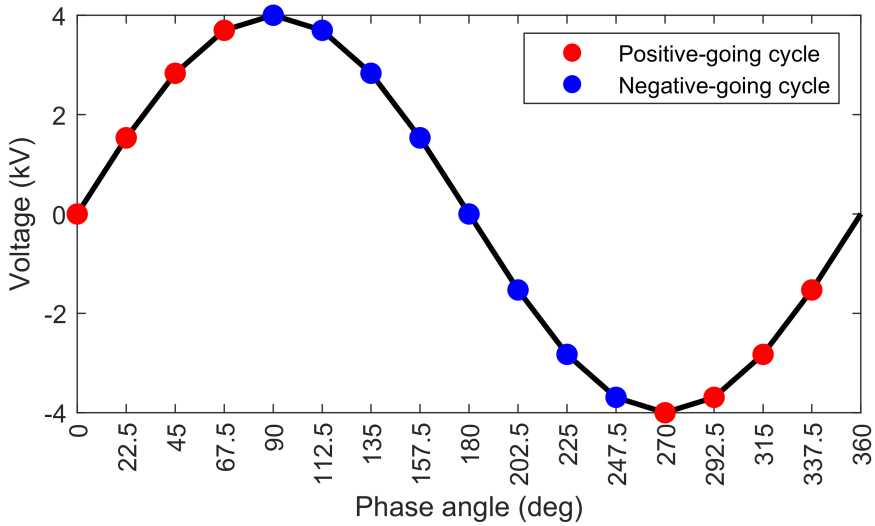

Figure 4.10: Schematic of negative and positive going strokes in an actuation cycle resolved at 16 phases.

The spatial distribution of the body force associated with the local acceleration term (from Equation (4.3) term(2)) during the negative going cycle is shown in Figure 4.8 (a) to (h) corresponding to a phase of 90° to 247.56°. The region in red corresponds to positive acceleration of the flow in the region. This can be seen initially developing at phase angle, $\phi = 90°$ between $x = 0$ mm and 3 mm.

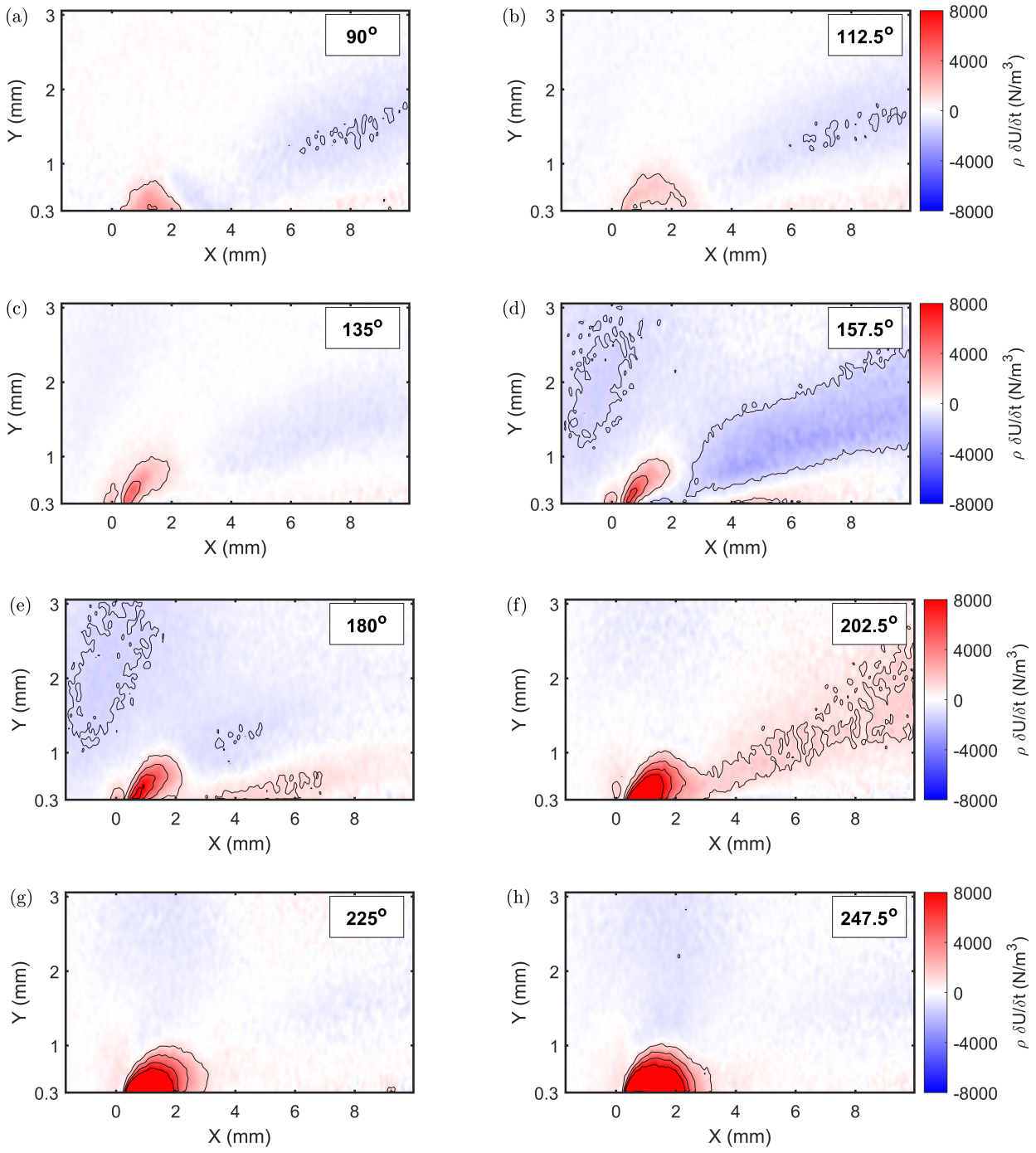

Figure 4.11: Spatial distribution of the local acceleration contribution during the negative-going cycle computed using term (2) of Equation 4.3, at $V_{pp} = 9$ kV and $f = 3$ kHz. Contour spacing of lines plotted, 2285.7 N/m^3.

This region of positive acceleration occurs at the downstream edge of the exposed electrode, in the region of plasma discharge. The region appears to be weak at $\phi = 90°$ and 112° and it appears to increase in magnitude and extent through the other phase angles, reaching its maximum ($\approx$ 15741 N/m^3) at $\phi = 247.5°$. This region of positive acceleration relates to the region in which negative ions accumulate over the plasma discharge. Previously published results [58, 59] have suggested that the positive body force, originates in the cloud of negatively charged particles close to the plasma actuator. Considering that the local acceleration term is the major contributor to the total body force production within the actuation cycle, it is reasonable to expect the local acceleration to develop similarly.

The spatial distribution of the local acceleration term in positive-going cycle of the actuation cycle is shown in Figure 4.12. The local acceleration continues to be positive at the beginning of the positive-going cycle, as seen in Figure 4.12(a). The positive acceleration region, however, is seen to reduce in intensity and be more concentrate near $x = 2$ mm at $\phi = 270°$. The inception of the negative acceleration region, depicted in blue, is observed at $\phi = 292.5°$, shown in Figure 4.12(b). This region expands in extent in both, x- and y-directions, and grows in intensity through the cycle from phase angle of 315° to 22.5°. The negative acceleration reaches its maximum value ($\approx$ -17152 N/m^3) at $\phi = 0°$. At phase angle of 45° the negative region is seen to lessen in intensity and the position of maximum intensity shifts downstream to $x = 2$ mm, similar to the behaviour observed at $\phi = 270°$. At the end of the cycle, at phase angle of 67.5°, a positive acceleration region begins to develop at the region between $x = 0$ mm and 2 mm, while a weakened negative acceleration region moves to the region between $x = 2$ mm and 3 mm. From there on the cycle repeats, and therefore when observed over a number of cycles, the local acceleration has no major contribution to the body force as the flow accelerates and decelerates in a similar manner within an actuation cycle.

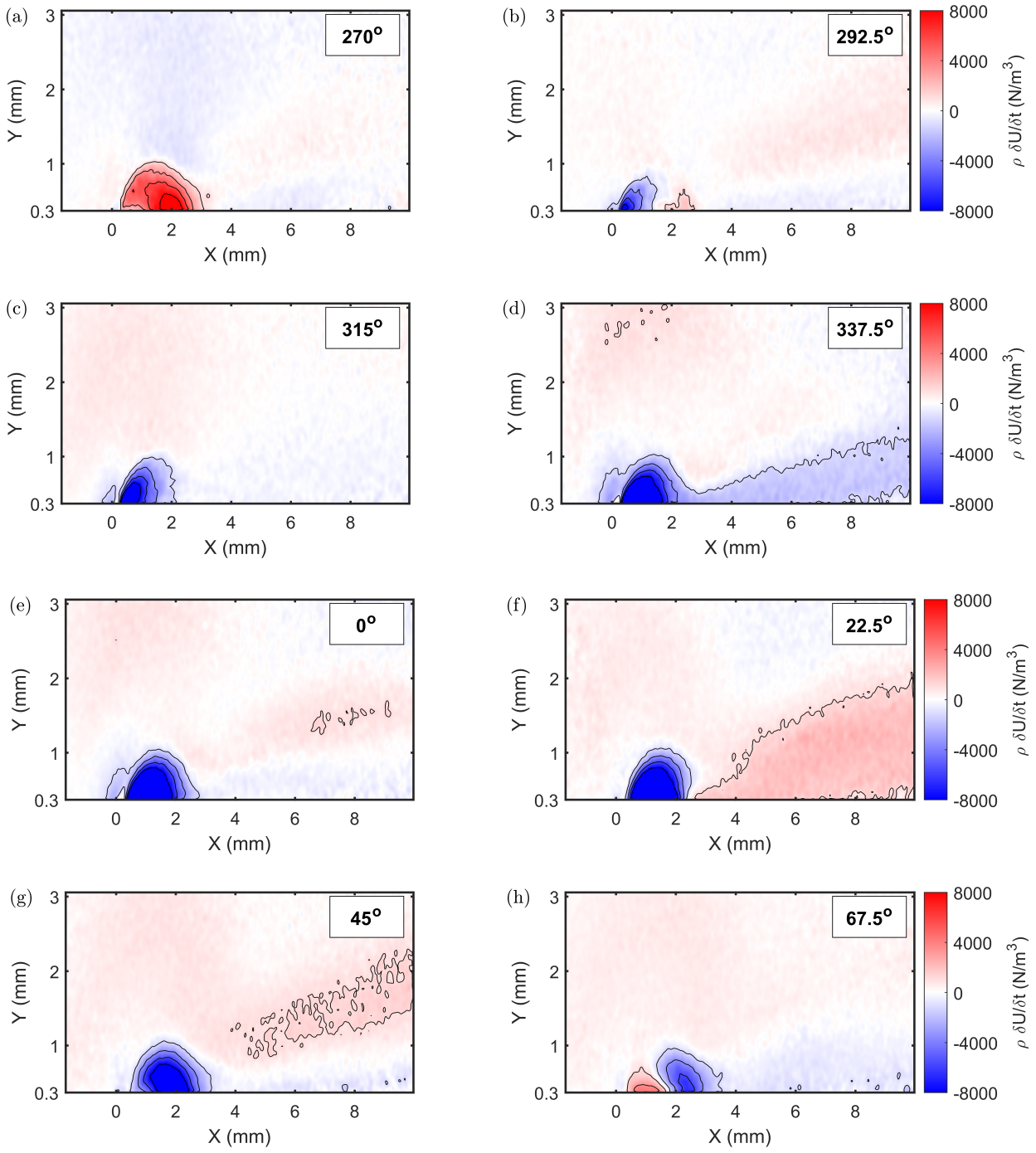

Figure 4.12: Spatial distribution of the local acceleration contribution during the positive-going cycle computed using term (2) of Equation 4.3, at $V_{pp} = 9$ kV and $f = 3$ kHz. Contour spacing of lines plotted, 2285.7 N/m^3.

4.8 Effect of Operating Conditions on Body Force

The velocity profiles of the horizontal component of the induced velocity, U_x, for different voltages for an operating frequency, $f = 3$ kHz at a downstream distance of $x = 6$ mm, is displayed in Figure 4.13. The velocity profiles shown in the figure are obtained by averaging the velocity fields over 16 phases of the actuation cycle. It can be observed that for higher operating voltages, the magnitude of induced velocity increases. As the operating voltage of the plasma actuator is increased, the strength of the electric field also increases. The increase in electric field translates to a higher energy plasma generated, which further increases the number of particle collisions and momentum transfer to the surrounding air. This leads to higher induced velocity and body force. The increase in maximum induced velocity with the voltage was noted to be non-linear similar to that observed in previous studies [52, 50, 54].

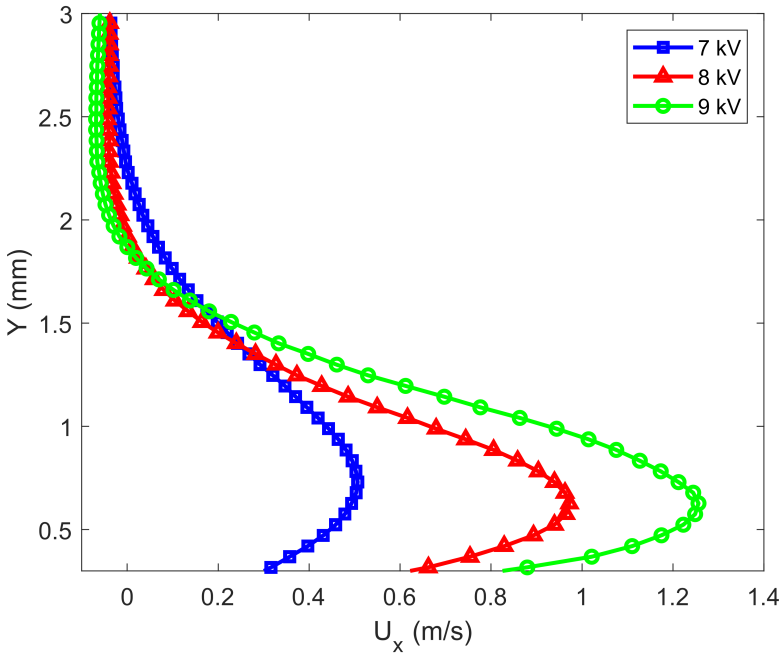

Figure 4.13: Velocity profiles of horizontal component of velocity, U_x, at $f = 3$ kHz and (a) 7 kV, (b) 8 kV, and (c) 9 kV at a downstream distance of $x = 6$ mm.

The spatial distribution of the mean horizontal volume force component, $\langle f_x \rangle$, for three voltages, 7, 8 and 9 kV are depicted in Figure 4.14(a), (b) and (c), respectively. It can be seen that the positive region near the discharge seems to increase in intensity and extent as the applied voltage is increased.

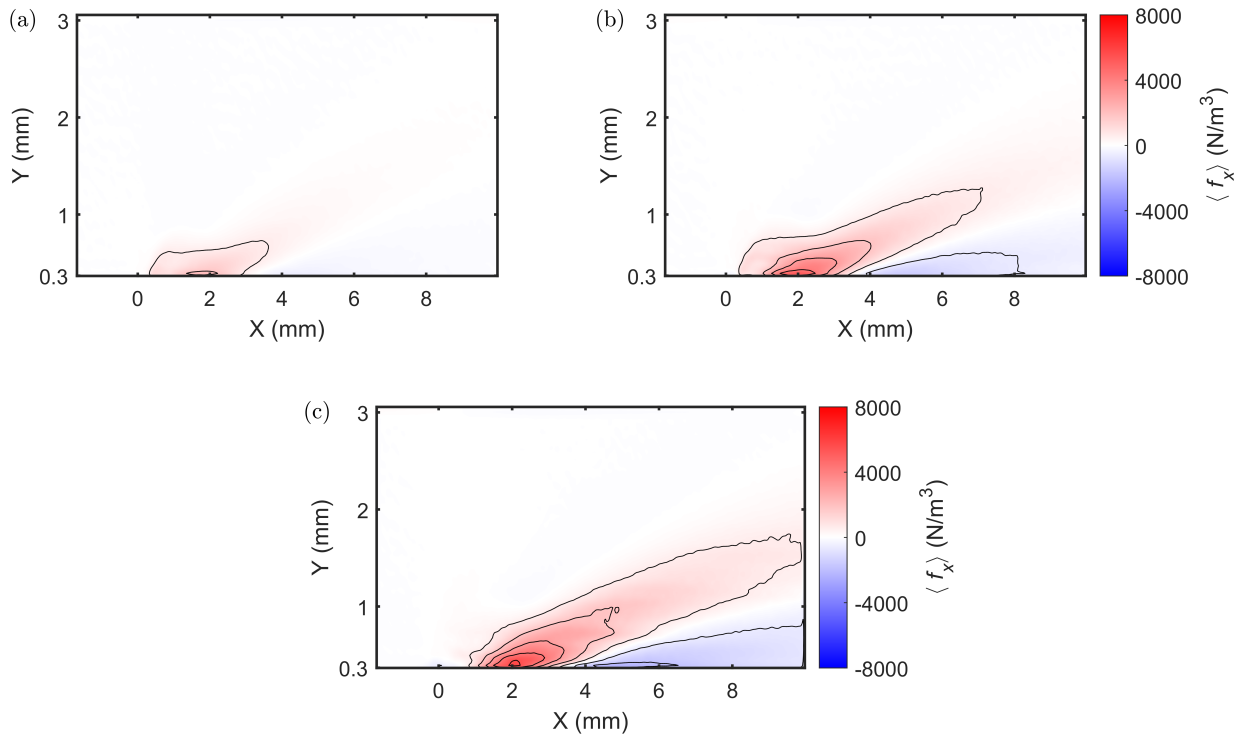

Figure 4.14: Spatial distribution of mean horizontal component of volume force, $\langle f_x \rangle$, calculated from Equation 4.3, at $f = 3$ kHz and (a) 7 kV, (b) 8 kV, and (c) 9 kV. Contour spacing of lines plotted, 1230.8 N/m^3.

Previous studies [5, 18] have confirmed that operating frequency is one of the parameters the magnitude of induced velocity and body force of the plasma actuator depends on. They concluded that the induced velocity and body force increased with increase in operating frequency, and plateaued after a certain threshold frequency, thereby noting the variation was non-linear. Figure 4.15 shows the velocity profiles of the horizontal component of the induced velocity, U_x, obtained in the present work, when a voltage of 9 kV was applied across the electrodes at an operating frequency of 2 kHz and 3 kHz. The velocity profiles obtained are a resultant of averaging the velocity fields over 16 phases of the actuation cycle. It can be seen that the induced velocity is higher for the higher operating frequency, i.e. 3 kHz.

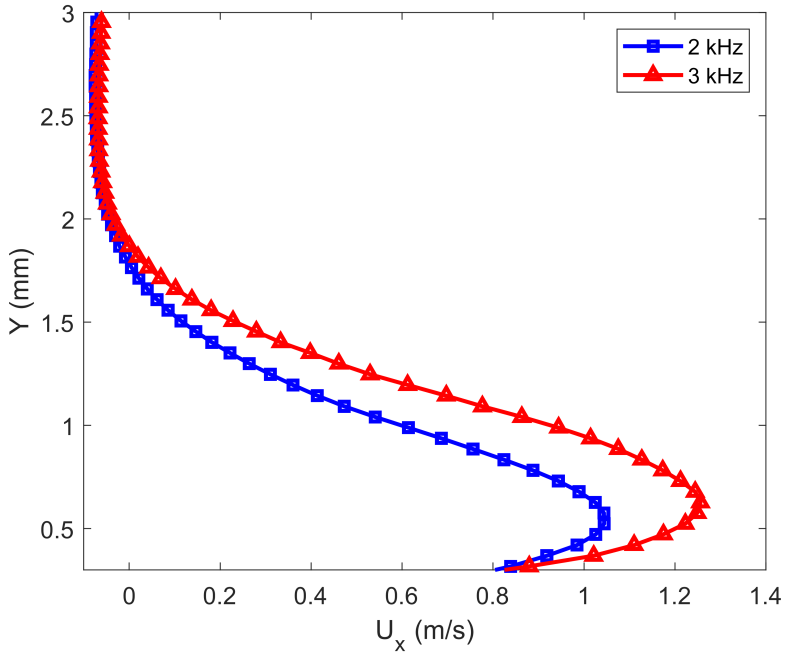

Figure 4.15: Velocity profiles of horizontal component of velocity, U_x, at $V_{pp} = 9$ kV and (a) 2 kHz, and (b) 3 kHz at a downstream distance of $x = 6$ mm.

Figure 4.16(a) and (b) shows the spatial distribution of the mean horizontal force component, $\langle f_x \rangle$, which was calculated using Equation (4.3), for the two different frequencies of 2 kHz and 3 kHz, respectively. The positive horizontal force region is observed to be stronger in the case of higher frequency, as expected. The extent of the volume force, as inferred from the first level (of approximately 1200 N/m^3), passes beyond $x = 8$ mm for the higher operating frequency.

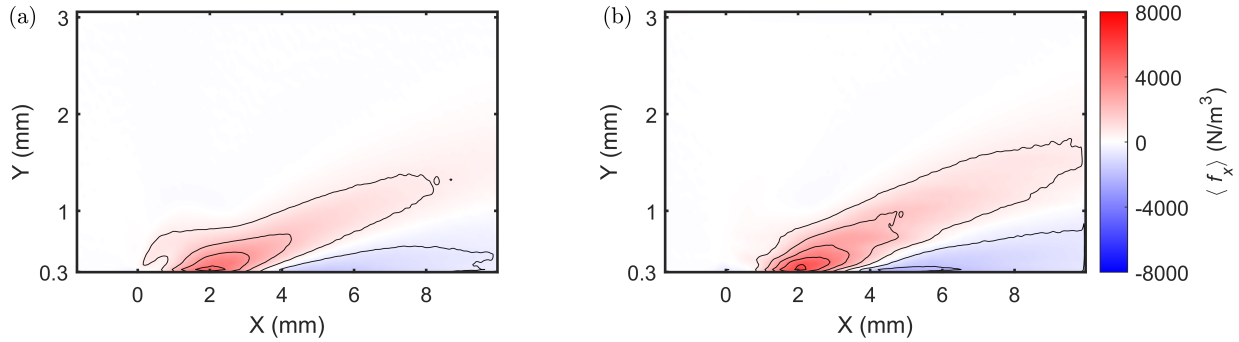

Figure 4.16: Spatial distribution of mean horizontal component of volume force, $\langle f_x \rangle$, calculated from Equation 4.3, at $V_{pp} = 9$ kV and (a) 2 kHz, and (b) 3 kHz. Contour spacing of lines plotted, 1230.8 N/m^3.

Chapter 5

Effect of Phase Resolution

5.1 Overview

In the present work, the velocity data were acquired at various phases of the sinusoidal voltage signal applied to the actuator. The data were acquired at 8 phases, 16 phases and 32 phases. The methodology of acquiring phase resolved data can be found in Section 3.4. In this chapter, the effect of the phase resolution for the current setup is studied. In the first section, data averaged over different phase resolutions are examined by observing the spatial distribution of the volume force. The effect of using various differencing methods in computing the derivatives of the momentum equations was also investigated. In the final section, the effect of phase resolution on the data is quantified. The data were acquired at a frequency of 1 kHz for all voltages (V_{pp} = 7-9 kV) for the work presented in this chapter.

5.2 Spatial Distribution of Time-Averaged Force at Different Phase Resolution

The spatial distribution of the horizontal component of the volume force, f_x is calculated using Equation 4.3, and averaged averaged over 8 phases, $\langle f_x \rangle_8$, 16 phases, $\langle f_x \rangle_{16}$, and 32

phases, $\langle f_x \rangle_{32}$, is shown in Figure 5.1(a), (b) and (c), respectively. The plasma actuator was operated at a voltage of 8 kV and frequency of 1 kHz. The total sample size for all the averaged phase data ($\approx$ 2000 image pairs) was maintained to eliminate the effect of noise.

On observing the spatial distribution of volume force, over three different phase resolutions, it can be seen that distribution exhibits some variation when averaged over different number of phases. The region near the plasma discharge, $x = 0$ mm to 2 mm, appears to be better resolved in the 16 phase and 32 phase data as compared to the 8 phase data. This suggests that the phase resolution of the data acquired has an effect on the spatial distribution of the force, and is significant, closer to the region of discharge. This effect can also be expected to be seen in the spatial distribution of its constituent terms. However, the magnitude of the force is seen to be nearly constant in Figure 5.1(a), (b) and (c).

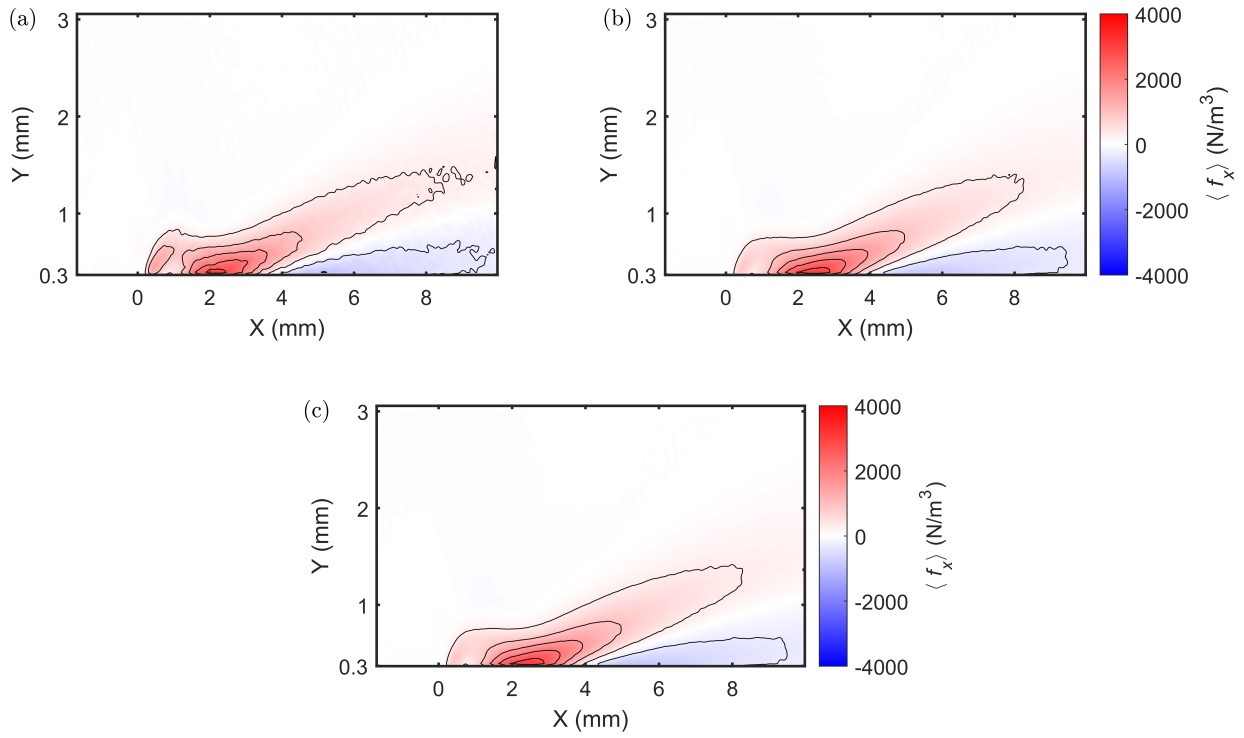

Figure 5.1: Spatial distribution of mean horizontal component of volume force, $\langle f_x \rangle$, calculated from Equation 4.3, at $V_{pp} = 8$ kV and $f = 1$ kHz for (a) 8 phases, (b) 16 phases, and (c) 32 phases. Contour spacing of lines plotted, 615.4 N/m^3.

Similarly, the spatial distribution of the force at an operating voltage of 9 kV is shown in Figure 5.2(a), (b) and (c). The distribution had similar characteristics to that observed when the plasma actuator was operated at 8 kV. The force distribution in between $x = 0$ mm and 2 mm, is again seen to be better resolved as the number of phases averaged over, increases.

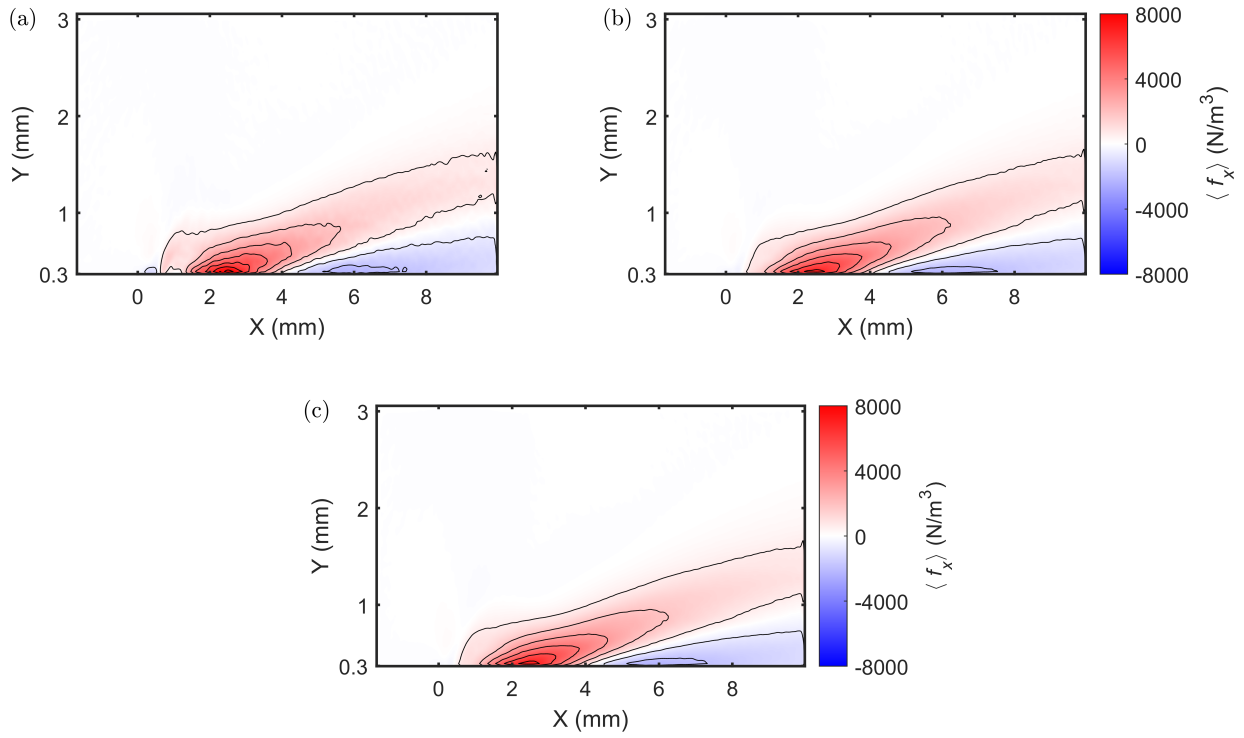

Figure 5.2: Spatial distribution of mean horizontal component of volume force, $\langle f_x \rangle$, calculated from Equation 4.3, at $V_{pp} = 9$ kV and $f = 1$ kHz for (a) 8 phases, (b) 16 phases, and (c) 32 phases. Contour spacing of lines plotted, 1230 N/m^3.

In order to quantify these observations, the 8 phase and 16 phase averaged data were subtracted from the 32 phase averaged data are shown in Figure 5.3(a) and (b), respectively. In Figure 5.3(a), the difference between 32 phase data and 8 phase data, $\langle f_x \rangle_{32} - \langle f_x \rangle_8$, can be seen to be much higher as compared to the difference between 32 phase data and 16 phase data, $\langle f_x \rangle_{32} - \langle f_x \rangle_{16}$, in Figure 5.3(b). It must be noted that the two plots have different colorbar scales. The variation in the distribution is seen to be significant close to the wall, between $x = 0$ mm and 6 mm.

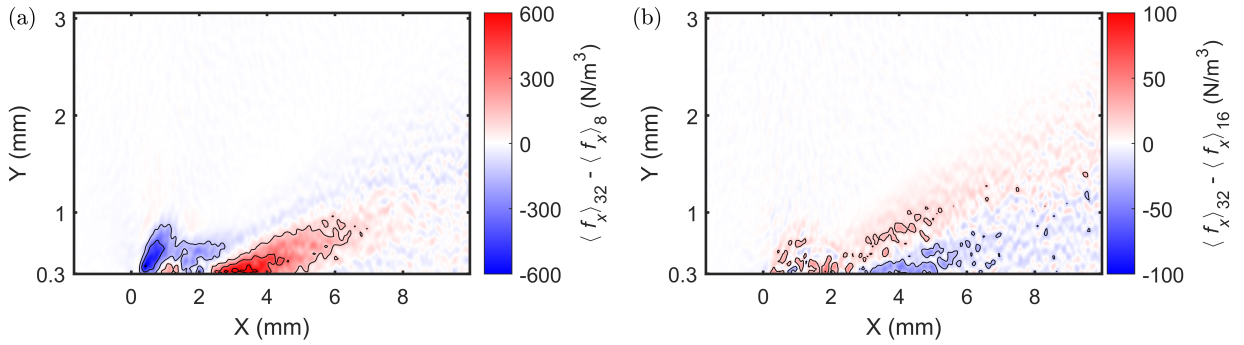

Figure 5.3: Difference between the spatial distribution of mean horizontal component of volume force, $\langle f_x \rangle$ averaged over phases, (a) $\langle f_x \rangle_{32} - \langle f_x \rangle_8$, (b) $\langle f_x \rangle_{32} - \langle f_x \rangle_{16}$ at $V_{pp} = 8$ kV. Contour spacing of lines plotted, (a) 240 N/m^3, (b) 40 N/m^3.

Similar contour plots for the data acquired at 9 kV of operating voltage is shown in Figure 5.4. The plots are shown in the same scale as in the Figure 5.3. It can be observed in both the plots in Figure 5.4, that the contours extend further in both x- and y-directions as compared to Figure 5.3. The differences between the 32 phase data and the other phase data increases with the increase in magnitude of the force. This suggests that the effect of phase resolution becomes more prominent as the force increases.

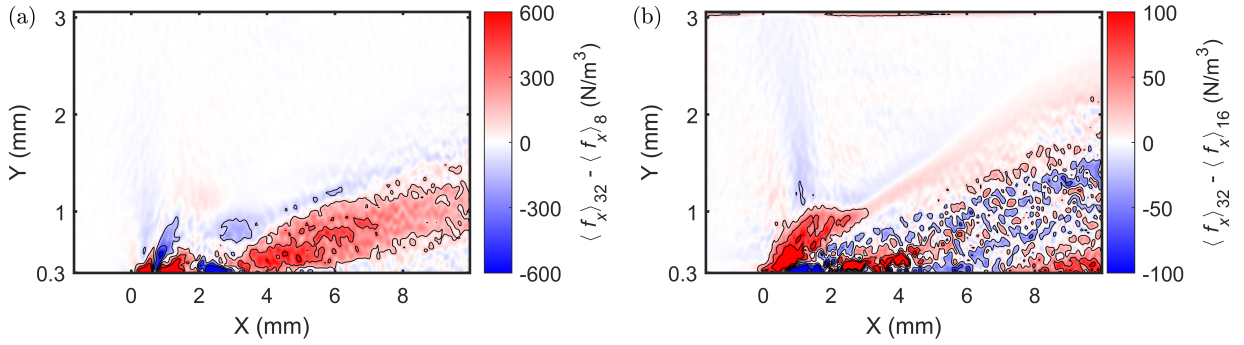

Figure 5.4: Difference between the spatial distribution of mean horizontal component of volume force, $\langle f_x \rangle$ averaged over phases, (a) $\langle f_x \rangle_{32} - \langle f_x \rangle_8$, (b) $\langle f_x \rangle_{32} - \langle f_x \rangle_{16}$ at $V_{pp} = 9$ kV. Contour spacing of lines plotted, (a) 240 N/m^3, (b) 40 N/m^3.

5.3 Effect of Phase Resolution on Body Force

The magnitude of the horizontal component of body force, F_x is plotted for 8 phase, 16 phase and 32 phase data in Figure 5.5. The magnitude of this force was determined using,

$$F_{x_n} = \iint_S \langle f_x(x, y, t) \rangle_{n=8,16,32} \, \mathrm{d}x\mathrm{d}y, \tag{5.1}$$

where, F_x, is determined from spatially integrating the force field obtained by averaging 8, 16 and 32 phases.

The horizontal axis of Figure 5.5 displays the number of phases over which the body force is calculated and the vertical axis shows the scale of the force, F_x. The difference between the 32 phase data and 16 phase data, Δf_1, is 0.12 mN/m. And the difference between the magnitudes of the force with 16 phases and 8 phases resolution, Δf_2 is 0.7 mN/m.

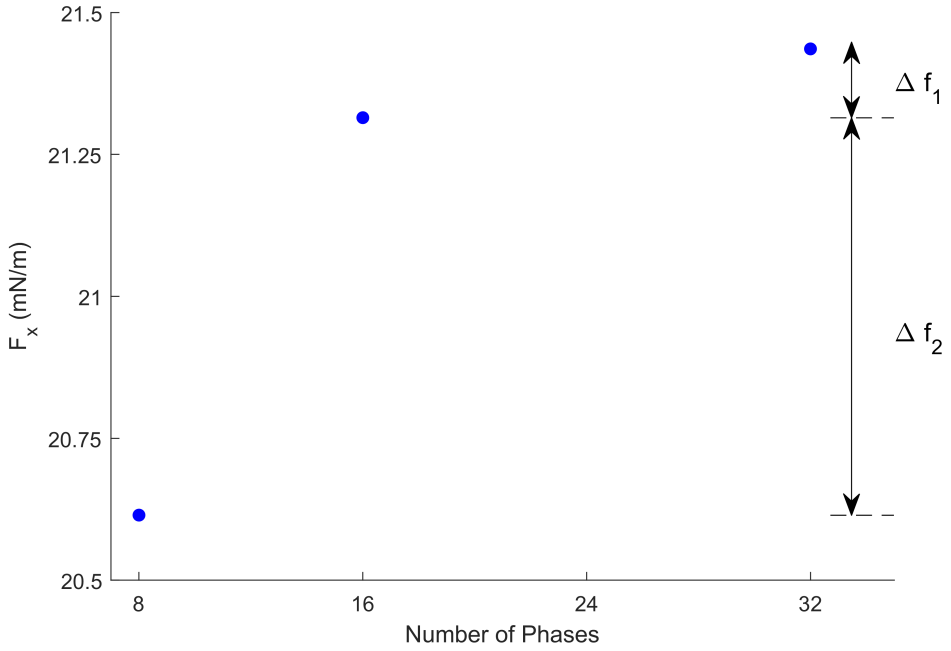

Figure 5.5: Comparison of the horizontal component of the body force, F_{x_n}, computed using Equation 5.1 over 8 phases, 16 phases and 32 phases at $V_{pp} = 8$ kV and $f = 1$ kHz.

The magnitude of the force at 16 phases was 3.5% higher than that of its magnitude at 8 phase. In comparison, the value of force at 32 phases was 0.5% higher than that at 16 phases.

Similar calculations were done for body force magnitudes at operating voltage of 9 kV and frequency of 1 kHz, shown in Figure 5.6, where the value of 32 phase data was observed to be 4.85% higher than its 16 phases value. And, the 16 phase data was 8.1% higher than that of the 8 phase data. This further consolidates the need for a higher phase resolution.

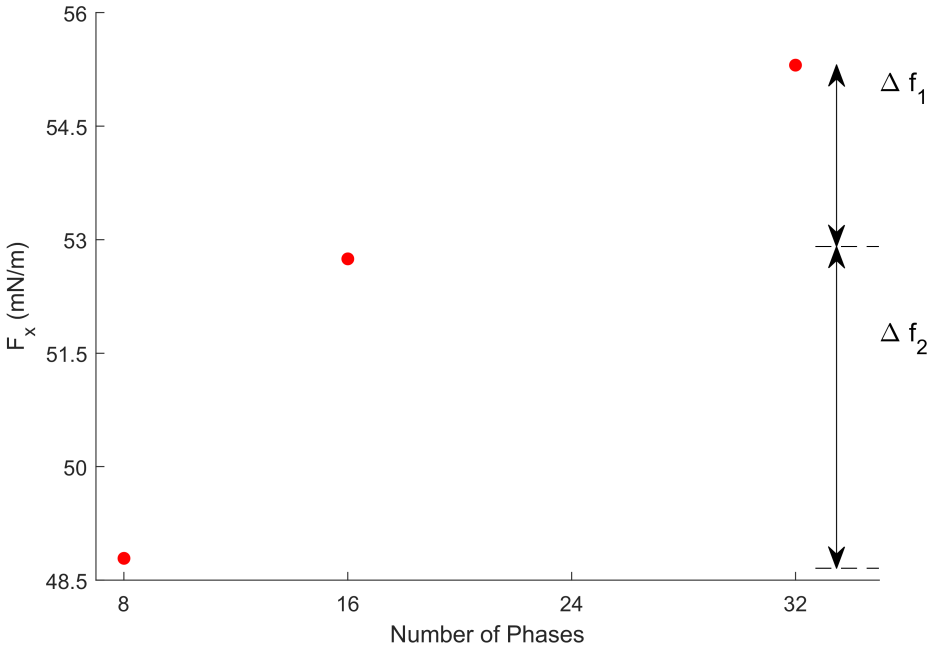

Figure 5.6: Comparison of the horizontal component of the body force, F_{x_n}, computed using Equation 5.1 over 8 phases, 16 phases and 32 phases at $V_{pp} = 9$ kV and $f = 1$ kHz.

5.4 Comparison of Phase Resolution

The phase resolution has a significant effect in capturing the variation of the body force within the actuation cycle. The variation of the body force with the phase angle, for different phase resolution is shown in Figure 5.8. The body force was generated by the actuator operated at

an applied voltage of 8 kV and frequency of 1 kHz. The peaks of forcing in each half-cycle of actuation can not be distinguished when the forcing is resolved only at 8 phases in the actuation cycle. The 16 phase data does provide a better understanding of the forcing, and provides a trend, as compared to the 8 phase data. The 32 phase resolved data appears to capture the unsteady nature of the force better, as compared to the 16 and 8 phase data.

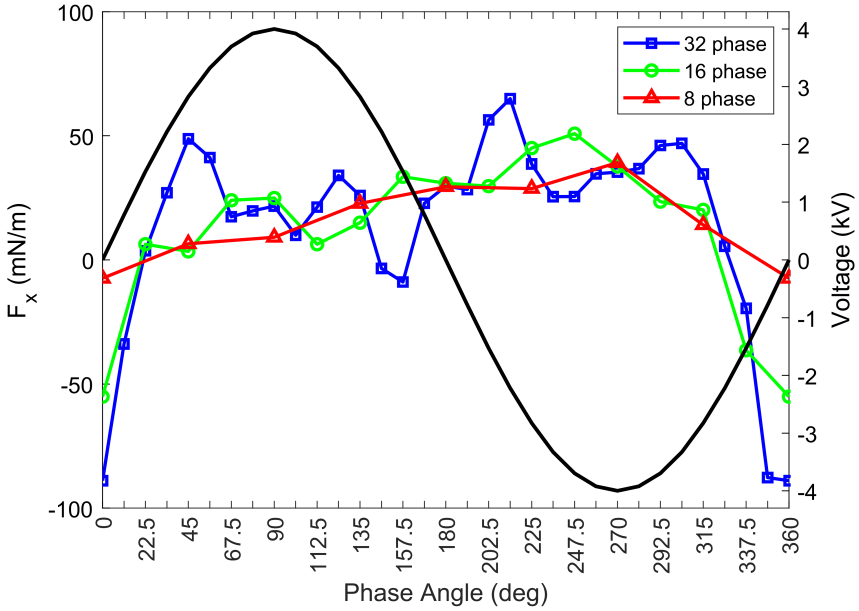

Figure 5.7: Comparison of the effect of phase resolution on the horizontal component of the body force, F_x, calculated from Equation 4.3, at $V_{pp} = 8$kV and $f = 1$ kHz.

5.5 Comparison of Differencing Schemes

The momentum equations is applied to the velocity fields in a discretised form to understand the momentum transfer between phases of actuation. Conventionally, a second-order central differencing scheme is used to discretize the equations and determine the forcing. In this work, three different differencing schemes were applied in an effort to understand their effect on the magnitude.

The equations of the three second order differencing schemes applied to discretize the momentum equations (given by Equations 4.3 and 4.4), are shown below.

Forward differencing scheme:

$$f'(x) = \frac{-3f(x) + 4f(x + \Delta x) - f(x + 2\Delta x)}{2\Delta x} \tag{5.2}$$

Central differencing scheme:

$$f'(x) = \frac{f(x + \Delta x) - f(x - \Delta x)}{2\Delta x} \tag{5.3}$$

Backward differencing scheme:

$$f'(x) = \frac{3f(x) - 4f(x - \Delta x) + f(x - 2\Delta x)}{2\Delta x} \tag{5.4}$$

These differencing schemes were used to calculate the first- and second-derivatives with respect to time or spatial coordinates in Equation 4.3, form which the body force was computed using Equation 4.5. The resulting body force, F_x, obtained by applying the three different differencing schemes is shown in Figure 5.8. The body force was calculated for the flow induced by actuator being operated at 8 kV and and 1 kHz. It can be seen that with the application of the forward and backward differencing schemes, there are oscillations in body force, that do not appear with the application of central differencing scheme. The central differencing scheme being the mathematical average of the forward and backward differencing scheme, applying it to the momentum equation (given by eq. 4.3), leads it to have a smoother profile of resulting F_x in comparison. The reason for the noise could be that the forward and backward differencing schemes apply the values of velocity from the phases ahead and the phases behind, respectively. Based on this observation, the use of central differencing scheme appears to be ideal especially considering the other two differencing schemes show no significant shift in magnitude throughout the actuation cycle.

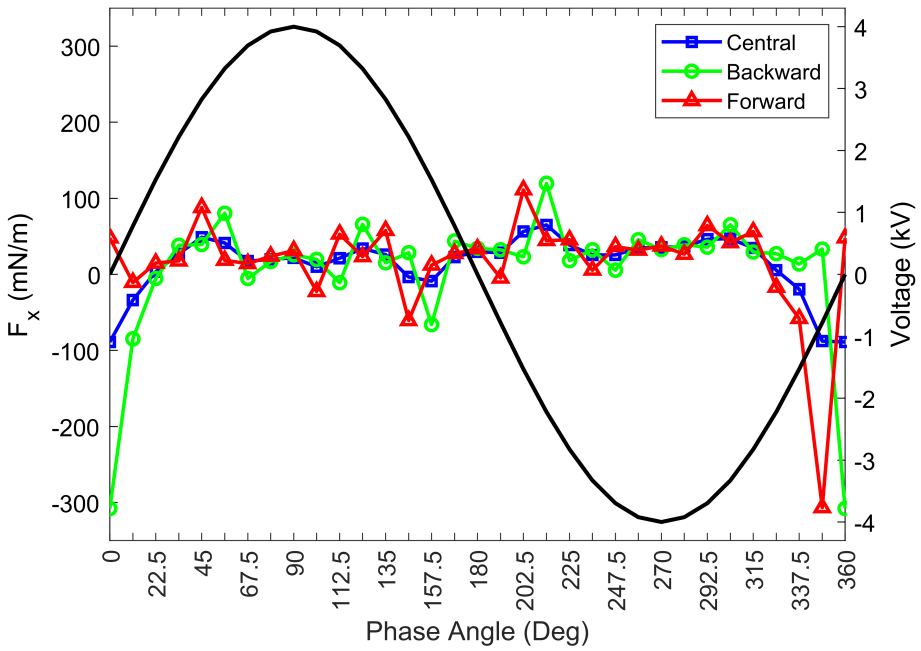

Figure 5.8: Comparison of differencing schemes applied to compute the horizontal component of the body force, F_x, calculated from Equation 4.3, at $V_{pp} = 8$ kV and $f = 1$ kHz.

5.6 Effect of Higher Order Differencing Schemes

Higher order differencing approximations are typically used to improve accuracy by reducing the truncation error. To observe if a higher order difference approximation of the derivatives had a significant effect on the final magnitude of the force obtained, a fourth order central differencing approximation was applied to the derivatives of the momentum equations.

$$f'(x) = \frac{-f(x+2\Delta x) + 8f(x+\Delta x) - 8f(x-\Delta x) + f(x-2\Delta x)}{12\Delta x} \tag{5.5}$$

The resulting body force is plotted along with the body force resulting from the application of second order central differencing approximations, in Figure 5.9.

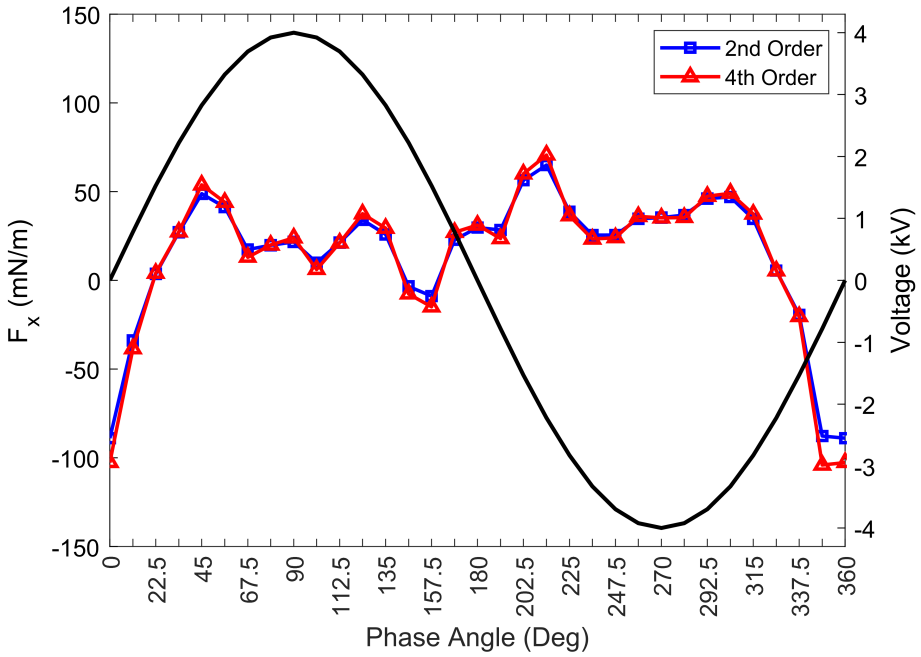

Figure 5.9: Comparison between different orders of central differencing schemes applied to compute the horizontal component of the body force, F_x at $V_{pp} = 8$ kV and $f = 1$ kHz.

It can be seen that applying a higher order differencing approximation does not have a notable effect on the body force. This suggests a second-order approximation sufficiently captures the variation of body force within an actuation cycle. The data displayed in the Figure 5.9 was acquired under the application of 8 kV of voltage, at a frequency of 1 kHz to the plasma actuator.

Chapter 6

Summary and Conclusions

In the present work, the phase resolved body force produced by a single dielectric barrier discharge actuator in a quiescent chamber of air was considered. To do so, the velocity field was sampled using phase-locked particle image velocimetry measurements. Interrogation of the velocity field data was used to determine the effect actuation on the terms decomposed from the discretized two-dimensional and incompressible momentum equations. Using this approach, it was possible to examine the nature of the wall jet generated and the spatial and temporal evolution of the aforementioned terms. Flow field data were acquired for operating voltages, V_{pp} = 7-9 kV and frequency, f = 1-3 kHz, at 8 phases, 16 phases, and 32 phases within the actuation cycle.

6.1 Phase Resolved Body Force Results

The velocity profiles at different downstream distances were observed to resemble and follow the theoretical, normalized velocity profile derived for a laminar wall jet described by Glauert [28]. The maximum induced velocity and the half jet width, were also seen to vary as, $U_m \propto x^{-0.46}$ and $\delta_{1/2} \propto x^{0.81}$, respectively, along the downstream distance, in close agreement with the theoretical predications of Schwarz *et al.* [57] and Glauert [28]. These findings establish the laminar wall-jet nature of the flow generated by plasma actuator in this study.

The body force of the plasma actuator was found to peak in the negative half-cycle of actuation and reach its minimum in the positive half-cycle, in accordance with previous studies [48, 5].

The local acceleration term was found to be the highest contributor to total force produced within an actuation cycle. The RMS value of local acceleration term was seen to be 89.6% of the RMS value of unsteady force production. On averaging over several cycles, the flow seems to become quasi-steady in nature and the effect of the local acceleration is seen to be insignificant because the flow accelerates and decelerates similarly within a cycle of actuation. The convective term was observed to be a dominant contributor to the body force over several cycle of actuation. It was found to contribute upto 96% of the total force in both the x- and y-components of the force.

The spatial and temporal evolution of the local acceleration term was also studied. It was observed that the behaviour of the local acceleration term was similar to that of the spatio-temporal evolution of body force observed by Benard *et al* [17]. This finding also corroborates the earlier finding that the local acceleration term is the dominant contributor to the body force within a cycle of actuation.

The effect of the operating conditions of the plasma actuator on the body force was briefly studied. It was observed that upon increasing the applied voltage, the induced velocity of the flow also increased. Similarly, an increase in operating frequency also resulted in increasing the induced velocity.

6.2 Effect of Phase Resolution

The PIV data were acquired at various phase resolutions of 8 phases, 16 phases and 32 phases. The spatial distribution of the force averaged over different number of phases, but equivalent sample size ($\approx$ 2000 image pairs) was examined. It was observed that spatial distribution of 8 phase data was not well resolved near the plasma discharge. This seemed to improve in the spatial distribution of force averaged over 16 phases and 32 phases. Similar

observations were made in the spatial distributions of the force upon increasing the applied voltage. Upon further investigation, it was found that the difference in force distribution was mainly in the region close to the plasma discharge and the wall. On increasing the voltage, the difference between the force distribution averaged over 32 phases and 8 phases, increased in extent and scale. This was also found true in the differences between the force distribution averaged over 32 phases and 16 phases. This suggested that effect of phase resolution becomes more prominent while observing forces of higher magnitude. It can also be stated that on increasing the phase resolution, a significant improvement in the spatial resolution of the force in the near-wall region.

The force fields averaged over 8, 16 and 32 phases were then spatially integrated to find the effect of phase resolution on the magnitude of the force. It was observed that the magnitude of force averaged over 32 phases was 0.5% higher than that of 16 phases, and 3.9% higher than 8 phases when the actuator was operated 8 kV of applied voltage. When the applied voltage was increased to 9 kV, the force averaged over 32 phases was found to be 4.85% higher than the 16 phases value, and 8.1% higher than that obtained by averaging over 8 phases. The increase in magnitude of the force achieved by averaging over 32 phases and 16 phases were significantly higher as compared to force averaged over 8 phases. This result emphasizes the importance of the temporal resolution on the evaluation of the volume force. The effect of number of phases on capturing the evolution of body force within the cycle of actuation was also investigated. It was found that the 32 phase resolved data captured the unsteady nature of the flow much better than the 16 phase and 8 phase resolved data.

The effect of applying various differencing schemes on momentum equations was also tested. It was observed that the second-order forward and backward differencing schemes produced an uncharacteristic variation in the body force resulting from the momentum equations. On the other hand, the central differencing appeared to be more stable, supporting its use to discretize the momentum equations as done by Benard *et al* [17]. It was also observed that increasing the order of differencing scheme from 2^{nd} order differencing approximation to 4^{nd} order differencing approximation produced no significant effect on magnitude of the body force.

6.3 Future Work

The plasma actuators are relatively new devices as compared to other active flow control devices. Though significant amount of research has been done on this device, the increasing applications of the device necessitates deeper understanding of their working under different operational parameters. In the future, it is recommended that the further studies on force production be performed over a range of operational conditions. An effort in understanding the behaviour and contribution of the aforementioned terms of momentum equations, under different operational and geometric parameters would be a key step towards improving the comparability and predictability of plasma actuator performance. It is also recommended to further investigate the importance of phase resolution while acquiring the data. Additional, 12 phase and 24 phase resolved data, would give a better understanding of the variation of force observed when averaging over several phases.

6.4 Concluding Remarks

The present work aims to enhance the understanding of body force production in plasma actuators and an optimal way of capturing it experimentally. Upon initially establishing the wall jet nature of the flow generated by the plasma actuator, the study was focused on understanding the contribution of the terms in the momentum equations to the total body force. This study also experimentally highlights the temporal behaviour of the dominant local acceleration term in the momentum equation, within a cycle of actuation. The importance of phase resolution while acquiring the data experimentally was also investigated.

In conclusion, the author wishes to emphasize on the importance of having a highly phase resolved data to study the transfer of momentum by the plasma actuators. The phase resolved measurements help in studying flow generated in an actuation cycle of a plasma actuator operated at high frequencies, where it generates pulsed velocity at the same frequency as the applied voltage. It is hoped that the present work contributes to the better understanding flow generated by the plasma actuators potentially leading to more applications and better numerical models to simulate them.

Bibliography

[1] J. Kriegseis, B. Simon, and S. Grundmann. Towards in-flight applications: a review on dielectric barrier discharge-based boundary-layer control. *Applied Mechanics Reviews*, 68(2):020802, 2016.

[2] L. N. Cattafesta and M. Sheplak. Actuators for active flow control. *Annual Review of Fluid Mechanics*, 43:247–272, 2011.

[3] R. E. Hanson, P. Lavoie, A. M. Naguib, and J. F. Morrison. Transient growth instability cancelation by a plasma actuator array. *Experiments in Fluids*, 49(6):1339–1348, 2010.

[4] A. Séraudie, O. Vermeersch, and D. Arnal. DBD Plasma actuator effect on a 2D model laminar boundary layer. Transition delay under ionic wind effect. *29th AIAA Applied Aerodynamics Conference*, 2011.

[5] A. Naghib-Lahouti, R. Pimentel, and P. Lavoie. (RTO) characterization of the time-dependent behaviour of dielectric barrier discharge plasma actuators. *45th AIAA Plasmadynamics and Lasers Conference*, 2014.

[6] E. Moreau. Airflow control by non-thermal plasma actuators. *Journal of Physics D: Applied Physics*, 40(3):605–636, 2007.

[7] J. R. Roth and D. M. Sherman. Boundary layer flow control with a one atmospere uniform glow discharge surface plasma. *AIAA Journal*, 1998.

[8] C. L. Enloe, T. E. McLaughlin, R. D. VanDyken, K. D. Kachner, E. J. Jumper, T. C. Corke, M. Post, and O. Haddad. Mechanisms and responses of a single dielectric barrier plasma sctuator: geometric effects. *AIAA Journal*, 42(3):595–604, 2004.

[9] U. Kogelschatz, B. Eliasson, and W. Egli. From ozone generators to flat television screens: history and future potential of dielectric-barrier discharges. *Pure and Applied Chemistry*, 71(10):1819–1828, 1999.

[10] U. Kogelschatz. Dielectric-barrier discharges: their history, discharge physics, and industrial applications. *Plasma Chemistry and Plasma Processing, Vol. 23, No. 1*, 23(1):5082–5093, 2003.

[11] N. M. Houser. Manufacturing of dielectric barrier discharge plasma actuator for degradation resistance. Master's Thesis, UTIAS, 2013.

[12] S. Wolf and M. Arjomandi. Investigation of the effect of dielectric barrier discharge plasma actuators on the radar cross section of an object. *Journal of Physics D: Applied Physics*, 44(31), 2011.

[13] C. O. Porter, J. W. Baughn, T. E. McLaughlin, C. L. Enloe, and G. I. Font. Plasma actuator force measurements. *AIAA Journal*, 45(7):1562–1570, 2007.

[14] G. I. Font. Boundary-layer control with atmospheric plasma discharges. *AIAA Journal*, 44(7):1572–1578, 2006.

[15] W. Kim, H. Do, M. G. Mungal, and M. A. Cappelli. On the role of oxygen in dielectric barrier discharge actuation of aerodynamic flows. *Applied Physics Letters*, 91(18):1–4, 2007.

[16] Orlov. Modelling and simulation of single dielectric barrier discharge plasma actuators. PhD thesis, Notre Dame, 2006.

[17] N. Benard, A. Debien, and E. Moreau. Time-dependent volume force produced by a non-thermal plasma actuator from experimental velocity field. *Journal of Physics D: Applied Physics*, 46(24), 2013.

[18] M. Forte, J. Jolibois, J. Pons, E. Moreau, G. Touchard, and M. Cazalens. Optimization of a dielectric barrier discharge actuator by stationary and non-stationary measurements

of the induced flow velocity: application to airflow control. *Experiments in Fluids*, 43(6):917–928, 2007.

[19] J. R. Roth and X. Dai. Optimization of the aerodynamic plasma actuator as an electrohydrodynamic (EHD) electrical device. *44th AIAA Aerospace Sciences Meeting*, 19:14604–14631, 2006.

[20] S. Grundmann and C. Tropea. Experimental damping of boundary-layer oscillations using DBD plasma actuators. *International Journal of Heat and Fluid Flow*, 30(3):394–402, 2009.

[21] X. Huang and X. Zhang. Streamwise and spanwise plasma actuators for flow-induced cavity noise control. *Physics of Fluids*, 20(3), 2008.

[22] J. Jolibois, M. Forte, and E. Moreau. Application of an AC barrier discharge actuator to control airflow separation above a NACA 0015 airfoil: optimization of the actuation location along the chord. *Journal of Electrostatics*, 66(9-10):496–503, 2008.

[23] M. P. Patel, T. T. Ng, S. Vasudevan, T. C. Corke, M. Post, T. E. McLaughlin, and C. F. Suchomel. Scaling effects of an aerodynamic plasma actuator. *Journal of Aircraft*, 45(1):223–236, 2008.

[24] A. V. Kozlov and F. O. Thomas. Bluff-body flow control via two types of dielectric barrier discharge plasma actuation. *AIAA Journal*, 49(9):1919–1931, 2011.

[25] S. Lemire, H. D. Vo, and M. W. Benner. Performance improvement of axial compressors and fans with plasma actuation. *International Journal of Rotating Machinery*, 2009.

[26] Y. H. Li, Y. Wu, M. Zhou, C. B. Su, X. W. Zhang, and J. Q. Zhu. Control of the corner separation in a compressor cascade by steady and unsteady plasma aerodynamic actuation. *Experiments in Fluids*, 48(6):1015–1023, 2010.

[27] J. G. Zheng, Y. D. Cui, J. Li, and B. C. Khoo. A note on supersonic flow control with nanosecond plasma actuator. *Physics of Fluids*, 30(4), 2018.

[28] M. B. Glauert. The wall jet. *Journal of Fluid Mechanics*, 1(06):625, 1956.

[29] P. Versailles, V. Gingras-Gosselin, and H. D. Vo. Impact of pressure and temperature on the performance of plasma actuators. *AIAA Journal*, 48(4):859–863, 2010.

[30] B. Wilke. Aerodynamic flow control by means of dielectric barrier discharge plasma actuators. PhD thesis, DLR Gottingen, 2009.

[31] T. Albrecht, T. Weier, G. Gerbeth, H. Metzkes, and J. Stiller. A method to estimate the planar, instantaneous body force distribution from velocity field measurements. *Physics of Fluids*, 23(2):10–14, 2011.

[32] J. Kriegseis, C. Schwarz, C. Tropea, and S. Grundmann. Velocity-information-based force-term estimation of dielectric-barrier discharge plasma actuators. *Journal of Physics D: Applied Physics*, 46(5), 2013.

[33] R. Durscher and S. Roy. Force measurement techniques and preliminary results using aerogels and ferroelectrics for dielectric barrier discharge actuators. *42nd AIAA Plasmadynamics and Lasers Conference*, 2011.

[34] A. R. Hoskinson, N. Hershkowitz, and D. Ashpis. Force measurements of single and double barrier DBD plasma actuators in quiescent air. *Journal of Physics D: Applied Physics*, 41(24), 2008.

[35] A. Hoskinson, N. Hershkowitz, and D. Ashpis. Comparisons of force measurement methods for DBD plasma actuators in quiescent air. *47th AIAA Aerospace Sciences Meeting*.

[36] J. W. Baughn, C. O. Porter, B. L. Peterson, T. E. McLaughlin, C. L. Enloe, G. I. Font, and C. Baird. Momentum transfer for an aerodynamic plasma actuator with an imposed boundary layer. *44th AIAA Aerospace Sciences Meeting*, 2006.

[37] C. L. Enloe, M. G. Mcharg, and T. E. Mclaughlin. Time-correlated force production measurements of the dielectric barrier discharge plasma aerodynamic actuator. *Journal of Physics D: Applied Physics*, 103:73302, 2008.

[38] M. Kotsonis, S. Ghaemi, L. Veldhuis, and F. Scarano. Measurement of the body force field of plasma actuators. *Journal of Physics D: Applied Physics*, 44(4), 2011.

[39] A. Debien, N. Benard, L. David, and E. Moreau. Unsteady aspect of the electrohydrodynamic force produced by surface dielectric barrier discharge actuators. *Applied Physics Letters*, 100:13901, 2012.

[40] A. Debien, N. Benard, L. David, and E. Moreau. Erratum: Unsteady aspect of the electrohydrodynamic force produced by surface dielectric barrier discharge actuators. *Applied Physics Letters*, 101(22):100–102, 2012.

[41] M. Neumann, C. Friedrich, J. Czarske, J. Kriegseis, and S. Grundmann. Determination of the phase-resolved body force produced by a dielectric barrier discharge plasma actuator. *Journal of Physics D: Applied Physics*, 46(4), 2013.

[42] F. O. Thomas, T. C. Corke, M. Iqbal, A. Kozlov, and D. Schatzman. Optimization of dielectric barrier discharge plasma actuators for active aerodynamic flow control. *AIAA Journal*, 2009.

[43] S. Grundmann and C. Tropea. Experimental transition delay using glow-discharge plasma actuators. *Experiments in Fluids*, 42(4):653–657, 2007.

[44] G. Borcia, C. A. Anderson, and N. M.D. Brown. Dielectric barrier discharge for surface treatment: Application to selected polymers in film and fibre form. *Plasma Sources Science and Technology*, 12(3):335–344, 2003.

[45] T. C. Manley. The electric characteristics of the ozonator discharge. *Transactions of The Electrochemical Society*, 84(1):83, 1943.

[46] J. Kriegseis, B. Möller, S. Grundmann, and C. Tropea. Capacitance and power consumption quantification of dielectric barrier discharge (DBD) plasma actuators. *Journal of Electrostatics*, 69(4):302–312, 2011.

[47] J. Kriegseis, B. Möller, S. Grundmann, and C. Tropea. On performance and efficiency of dielectric barrier discharge plasma actuators for flow control applications. *International Journal of Flow Control*, 4(3-4):125–131, 2012.

[48] J. Kriegseis. Performance characterization and quantification of dielectric barrier discharge plasma actuators. PhD thesis, Darmstadt, 2011.

[49] J. Pons, E. Moreau, and G. Touchard. Asymmetric surface dielectric barrier discharge in air at atmospheric pressure: electrical properties and induced airflow characteristics. *Journal of Physics D: Applied Physics*, 38:3635–3642, 2005.

[50] S. Okochi, N. Kasagi, Y. Suzuki, and S. Ito. Development of micro plasma actuator for active flow control. *7th World Conference on Experimental Heat Transfer, Fluid Mechanics and Thermodynamics*, 2009.

[51] J. Little, M. Nishihara, I. Adamovich, and M. Samimy. High-lift airfoil trailing edge separation control using a single dielectric barrier discharge plasma actuator. *Experiments in Fluids*, 48(3):521–537, 2010.

[52] C. L. Enloe, T. E. Mclaughlin, R. D. Vandyken, K. D. Kachner, E. J. Jumper, and T. C. Corke. Mechanisms and responses of a single dielectric barrier plasma actuator: plasma morphology. *AIAA Journal*, 42(3), 2004.

[53] B. Dong, J. M. Bauchire, J. M. Pouvesle, P. Magnier, and D. Hong. Experimental study of a DBD surface discharge for the active control of subsonic airflow. *Journal of Physics D: Applied Physics*, 41(15), 2008.

[54] J. P. Murphy, J. Kriegseis, and P. Lavoie. Scaling of maximum velocity, body force, and power consumption of dielectric barrier discharge plasma actuators via particle image velocimetry. *Journal of Applied Physics*, 113(24), 2013.

[55] R. E. Hanson, N. M. Houser, and P. Lavoie. Dielectric material degradation monitoring of dielectric barrier discharge plasma actuators. *Journal of Applied Physics*, 115(4), 2014.

[56] T. N. Jukes, K. So Choi, G. A. Johnson, and S. J. Scott. Characterization of surface plasma-induced wall flows through velocity and temperature measurements. *AIAA Journal*, 44(4):764–771, 2006.

[57] W. H. Schwarz and W. P. Cosart. The two-dimensional turbulent wall-jet. *Journal of Fluid Mechanics*, 10(04), 48, 1960.

[58] J. P. Boeuf, Y. Lagmich, and L. C. Pitchford. Contribution of positive and negative ions to the electrohydrodynamic force in a dielectric barrier discharge plasma actuator operating in air. *Journal of Applied Physics*, 106(2), 2009.

[59] S. Leonov, D. Opaits, R. Miles, and V. Soloviev. Time-resolved measurements of plasma-induced momentum in air and nitrogen under dielectric barrier discharge actuation. *Physics of Plasmas*, 17(11), 2010.